This is a repository copy of *Transmission electron microscopy of epitaxial semiconductor materials and devices*.

White Rose Research Online URL for this paper:
https://eprints.whiterose.ac.uk/218882/

Version: Accepted Version

Article:
Dong, J. orcid.org/0000-0002-3853-1910, Bai, H., Deng, Y. et al. (5 more authors) (2025) Transmission electron microscopy of epitaxial semiconductor materials and devices. Journal of Physics D: Applied Physics, 58 (4). 043001. ISSN 0022-3727

https://doi.org/10.1088/1361-6463/ad8a6b

© 2024 The Authors. Except as otherwise noted, this author-accepted version of a journal article published in Journal of Physics D: Applied Physics is made available via the University of Sheffield Research Publications and Copyright Policy under the terms of the Creative Commons Attribution 4.0 International License (CC-BY 4.0), which permits unrestricted use, distribution and reproduction in any medium, provided the original work is properly cited. To view a copy of this licence, visit http://creativecommons.org/licenses/by/4.0/

Reuse
This article is distributed under the terms of the Creative Commons Attribution (CC BY) licence. This licence allows you to distribute, remix, tweak, and build upon the work, even commercially, as long as you credit the authors for the original work. More information and the full terms of the licence here:
https://creativecommons.org/licenses/

Takedown
If you consider content in White Rose Research Online to be in breach of UK law, please notify us by emailing eprints@whiterose.ac.uk including the URL of the record and the reason for the withdrawal request.

eprints@whiterose.ac.uk
https://eprints.whiterose.ac.uk/

1
2
3
4
5
6
7
8
9
10
11
12
13
14
15
16
17
18
19
20
21
22
23
24
25
26
27
28
29
30
31
32
33
34
35
36
37
38
39
40
41
42
43
44
45
46
47
48
49
50
51
52
53
54
55
56
57
58
59
60

Transmission electron microscopy of epitaxial semiconductor materials and devices

Jiawei Dong[1*], Hongjie Bai[2], Yong Deng[3], Shuo Liu[1], Xiaoyi Wang[1#], Yang Qiu[4#], Yuechun Shi[5] and Thomas Walther[6]

[1] Southwest Minzu University, State Ethnic Affairs Commission, Chengdu 610041, China
[2] Public Security Department, Sichuan Police College, Luzhou 646000, PR China
[3] Department of Physics, Southern University of Science and Technology, Shenzhen 518055, China
[4] Pico Center, SUSTech Core Research Facilities, Southern University of Science and Technology, Shenzhen 518055, China
[5]Yongjiang Laboratory, Ningbo 315000, China
[6] Dept. Electronic & Electrical Eng., University of Sheffield, Sheffield S1 3JD, UK

Correspondence
Southwest Minzu University, State Ethnic Affairs Commission, Chengdu 610041, China; Email: 80300024@swun.edu.cn
Pico Centre, SUSTech Core Research, Facilities, Southern University of Science and Technology, Shenzhen 518055, China; Email: qiuy@sustech.edu.cn

Abstract:

The transmission electron microscope (TEM) is a powerful imaging, diffraction and spectroscopy tool that has revolutionized the field of microscopy. It has contributed to numerous breakthroughs in various scientific disciplines. TEM-based techniques can offer atomic resolution as well as elemental analysis, which benefit the study of epitaxial semiconductors and their related optoelectronic devices on the atomic scale. The design and optimization of the device performance depend on three key factors: the control of strain at nanometer scale, control of the formation and propagation of defects as well as the control of local electronic properties. Manipulation and optimization are only possible if the key factors can be characterized precisely. Herein, the TEM techniques for strain analysis, defect characterization and bandgap evaluation are reviewed and discussed. Lately, with the development of in-situ TEM techniques, researchers have been able to observe dynamic processes and study the behaviour of materials and devices under realistic conditions (in gaseous atmosphere or in liquids, at elevated or cryogenic temperatures, under strain, bias or illumination) in real-time with extremely high spatial resolution. This review explores the impact and significance of in-situ TEM in the field of semiconductors.

Keywords: epitaxial semiconductor materials, transmission electron microscopy, strain, defect, bandgap, in-situ TEM techniques

Accepted Manuscript

1
2
3
4
5
6
7
8
9
10
11
12
13
14
15
16
17
18
19
20
21
22
23
24
25
26
27
28
29
30
31
32
33
34
35
36
37
38
39
40
41
42
43
44
45
46
47
48
49
50
51
52
53
54
55
56
57
58
59
60

Outline:

1. Introduction

2. Strain analysis

3. Defect characterization

4. Evaluation of bandgap by VEELS

5. In-situ TEM techniques

6. Conclusion and outlook

1. Introduction

Epitaxial semiconductors play an important role in electronic and optoelectronic devices, such as transistors, light-emitting diodes (LEDs), solar cells and detectors [1]-[5]. Those devices are the core components of integrated electronic devices that can be used in the field of communications, green energy, aerospace, healthcare etc. Epitaxy, such as by molecular beam epitaxy (MBE) or metalorganic vapour phase epitaxy (MOVPE), is normally used to grow the layers for the active regions of the devices after a buffer layer has been deposited on a crystalline substrate, and the active regions of the devices can be structured by photo- and electron lithography afterwards [6],[7]. As these active device regions are sometimes only a few ten nanometres in lateral size and can be atomically thin, e.g. gate oxides in field-effect transistors, and may contain atomic defects that can alter the optoelectronic behaviour of the device, characterisation methods with sub-nanometre resolution, such as electron microscopy, are necessary to study them.

The substrate usually is a single-crystalline wafer, sliced from a semiconductor ingot. Commercially, silicon (Si) is the most common material for crystalline substrates. MBE is a physical deposition technique that works over a wide temperature range in ultra-high vacuum (UHV), while MOVPE is a chemical deposition technique that works at relatively high temperatures, allowing the precursors to effectively react. MBE enables the precision control of single atomic layer growth, which makes it an ideal choice for researching crystal structures and monitoring growth rates. In contrast, compared to film epitaxy using MBE, MOVPE, also named metal organic chemical vapour deposition (MOCVD), can deposit films over larger areas and exhibits a faster growth rate, making it more suitable for commercial applications [8]-[12].

Accepted Manuscript

1 2 3 4 5 6 7 8 9 10 11 12 13 14 15 16 17 18 19 20 21 22 23 24 25 26 27 28 29 30 31 32 33 34 35 36 37 38 39 40 41 42 43 44 45 46 47 48 49 50 51 52 53 54 55 56 57 58 59 60

Usually, high crystal quality can be expected from MOCVD, however, compared with MBE growth [13], the epilayer grown by MOCVD may contain more chemical impurities due to the lower vacuum in the deposition chamber. Ideally, high quality epilayers involve the consideration of uniformity, crystal quality and chemical composition of the thin film [14],[15]. To grow a high-quality thin film, multiple growth parameters must be understood and optimized, especially the strain field near the heterostructure interface. In case of epilayer uniformity, in the early stage of the growth (thickness of several atomic layers), significant elastic strain energy is accommodated near the heterostructure interface due to the lattice mismatch between substrate and epilayer, and the compressive strain field at the interface is responsible for turning the epitaxy from layer-to-layer growth to Stranski-Krastanov (S-K) growth, which increases the surface roughness of the thin film [16]-[18]. For crystal quality of the thin film, as the epilayer thickness exceeds the critical thickness, effective interface strain relaxation could induce the generation of misfit dislocations [19] so that the crystal quality deteriorates due to the increase of dislocation density. Normally, a lattice mismatched epitaxial buffer layer of sufficient thickness is deposited on top of the substrate prior to deposition of the device structure to confine the misfit dislocations to the interface between substrate and buffer. Therefore, the active region grown subsequently, which is far away from the interface, may not be impeded by misfit dislocations, however, threading dislocations can extend further upwards. Finally, regarding the growth of perfect compound semiconductors, for example, the growth of ternary InGaN alloys, the interface strain field may lead to the narrowing of the miscibility gap and shift it towards higher In content [20]. Therefore, without the quantification of interface strain contours, InGaN may suffer from In segregation [21] or phase separation [22] during thin film epitaxy, leading to the production of local In-rich/poor regions in the epilayer. Such In-rich regions or dislocations are able to trap local electrons [23],[24], which can lead to the degradation of the device performance or even failure of the device. To optimize the growth parameters for achieving high quality epilayers, it is crucial to accurately measure the strain contours, atomic structure of lattice defects and nanoscale electronic states near the interface of heterojunctions.

Conventionally, characterization techniques for semiconductor applications involve X-ray diffraction, atomic force microscopy, secondary ion mass spectroscopy, scanning electron microscopy, four-point electrical measurements and photoluminescence [25]. From a combination

Accepted Manuscript

of measurement results, the crystallography and electrical properties of semiconductors can be obtained. Nevertheless, to directly associate the crystalline quality and electrical performance via multi-scale characterization techniques is extremely difficult, especially for multi-layer III-nitride compound semiconductors [26]. For example, the type and density of structural dislocations, alloy phase separation, elemental segregation, 2D electron gas formation at interfaces and uniformity of doping could all play a role so it is often impossible to infer the impact of one type of defect alone on overall electrical properties **Error! Reference source not found.**-[29]. Therefore, to simultaneously reveal single defects and their corresponding electronic states, techniques able to probe multiple physical fields at nano-scale are desirable for semiconductor nanostructure characterization.

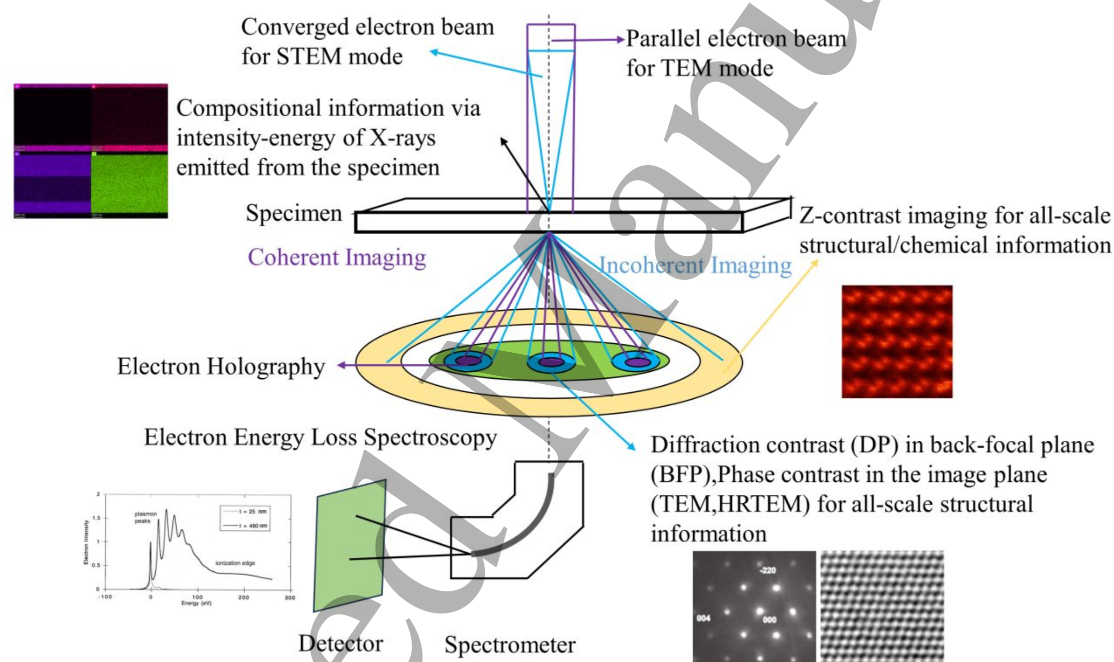

Fig.1. signals generated by the interaction of the primary electrons and material for studying the structural and electronic properties of semiconductor devices [30],[31].

TEM enables a direct probing of the nanostructure at atomic scale, revealing the atom arrangement within a certain nanostructure or local defect. Apart from imaging, analytical TEM can be used to perform chemical, strain and electronic state analysis [32]-[34]. All these techniques are based on the theory of electron-matter interaction [35]-[38]. If a parallel high-energy electron beam is used to irradiate a thin specimen, this is commonly called TEM

Accepted Manuscript

1 2 3 4 5 6 7 8 9 10 11 12 13 14 15 16 17 18 19 20 21 22 23 24 25 26 27 28 29 30 31 32 33 34 35 36 37 38 39 40 41 42 43 44 45 46 47 48 49 50 51 52 53 54 55 56 57 58 59 60

mode. Bright-field (BF) images, dark-field (DF) images, high-resolution (HR) TEM images, diffraction patterns (DPs), energy dispersive X-ray spectra (EDXS) and electron energy loss spectroscopy (EELS) data can be recorded (Figure 1), some of them simultaneously. The images and spectra can be used to study the local structure, crystallography, chemistry and electronic states [39]-[42]. TEM also can be operated in scanning transmission electron microscopy (STEM) mode, where a finely focused convergent electron beam has been formed to raster across the sample [43]-[45]. In the last decade, with the development of spherical aberration correction [46] and improvements of the electron gun [47], the spatial resolution of STEM can now approach ~50 pm (pm $=10^{-12}$m). High-angle annular dark field (HAADF) images, annular bright field (ABF) images, and BF images can be recorded simultaneously, and with a special segmented annular detector, differential phase contrast (DPC) images and integral differential phase contrast (iDPC) images [48]-[50] can also be generated to study the electromagnetic field distribution and light element arrangement within the scanned area, respectively. Moreover, by combining STEM with various detectors, detailed high-resolution maps can be formed easily, providing multi-physics characterization of the region of interest (ROI), such as EDXS mapping [51], EELS mapping [52], nano-beam electron diffraction (NBED) mapping [53], convergent beam electron diffraction (CBED) mapping [54], and four-dimensional (4D) STEM [55].

Recently, the development of in-situ TEM techniques has allowed the access of external stimulation induced nanostructure response at different time intervals. This capability provides information on materials dynamics in particular environments, such as crystal growth, phase transitions and defect formation [56],[57]. It also allows for the precise characterization of semiconductor materials under multiple external fields, such as variations in temperature, pressure, or electrical bias, which render a deep understanding of the structural and electronic properties of the devices. In addition, in-situ TEM techniques enable the direct diagnosis of failure processes of devices under certain working environments, providing valuable information for developing more reliable devices [58].

To perform an ideal TEM measurement using both imaging and spectroscopy, the preparation of a high quality TEM specimen is necessary. In the field of epitaxial semiconductors, two methods are usually applied to produce electron transparent thin foils:

1. Mechanical grinding and polishing, followed by Ar^{+} ion milling for final thickness

Accepted Manuscript

1
2
3
4
5
6
7
8
9
10
11
12
13
14
15
16
17
18
19
20
21
22
23
24
25
26
27
28
29
30
31
32
33
34
35
36
37
38
39
40
41
42
43
44
45
46
47
48
49
50
51
52
53
54
55
56
57
58
59
60

reduction and surface polishing [59]-[62],

2. Focused ion beam (FIB) milling for TEM lamella preparation.

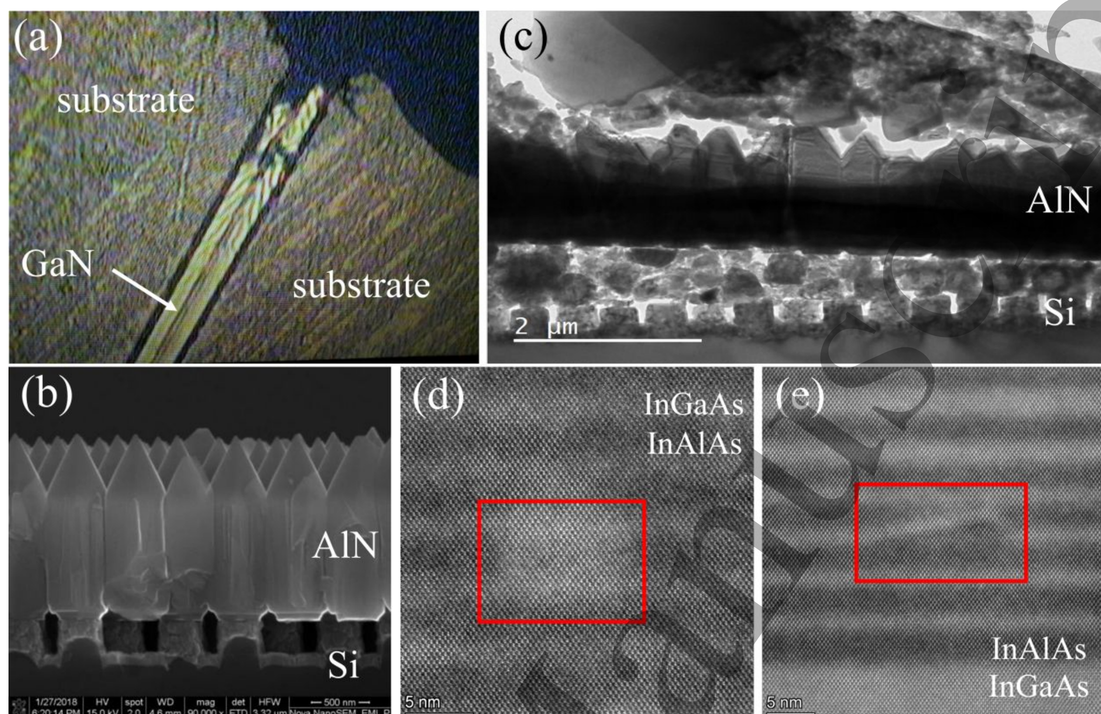

Fig.2. (a) GaN based TEM specimen prepared by method 1. (b) Epitaxial lateral overgrowth of AlN on Si. (c) Delamination of Si and AlN during the mechanical grinding. (d) Ga^+ implantation induced In segregation in InGaAs, (e) Loss of local atomic order in a Ga^+ ion-beam-damaged sample.

For producing high quality TEM samples via method 1, mechanical grinding and polishing by using a tripod polisher is desirable [63]. Compared with the planar grinding approach (where the critical thickness of fracture for GaN is typically ~15 μm), the sample thickness can be reduced to ~2 μm (GaN based semiconductors) before Ar^+ ion milling, so the ion-bombardment induced structural damage can be minimized due to the limited duration of ion milling [64]. Besides, the electron transparency after ion milling can be easily recognized, once orange-purple thickness fringes are noticed in optical imaging (Fig 2 (a)), indicating that the sample is sufficiently thin for TEM measurement [65]. However, mechanical sample preparation is extremely time consuming, especially at the final polishing stage as the sample thickness should be checked frequently to avoid any fracture or damage in the region of interest. Particularly, for grinding nanowires or

Accepted Manuscript

1
2
3
4
5
6
7
8
9
10
11
12
13
14
15
16
17
18
19
20
21
22
23
24
25
26
27
28
29
30
31
32
33
34
35
36
37
38
39
40
41
42
43
44
45
46
47
48
49
50
51
52
53
54
55
56
57
58
59
60

epitaxial thin films grown on patterned substrates, care must be taken to avoid the local splitting of substrate and epilayer (Fig 2 (b) and (c)) which could further increase the duration for preparing TEM specimens. To improve the efficiency of TEM specimen preparation, the use of focused ion beam systems could be a solution. The typical steps that involve the preparation of TEM specimen lamellas are [66],[67]: (a) identification of the region of interest (ROI), (b) bringing the specimen to eucentric height, (c) platinum deposition using a gas injection system (GIS) (initial decomposition by the electron beam, then by the gallium ion beam) over the ROI, (d) ion milling (with gallium ions at ~30 kV) to produce the lamella by forming trenches adjacent to the platinum coated region, (f) transferring the lamella onto the TEM grid, (g) thinning the specimen down to ~100 nm with 2 kV ion beam, where a low (~9 pA) beam current is often used to avoid further ion implantation. Compared with traditional sample preparation techniques, FIB can precisely control the position and shape of the ion beam, extract specific nanostructures from the sample and achieve uniform sample thickness. In combination with Electron Back-Scatter Diffraction (EBSD) measurements before lamella extraction [68], FIB can extract lamellas with specific preferetnial orientations. However, the collision of the Ga^+ ion beam on the surface of the sample during FIB processing always causes some Ga^+ implantation damage, including chemical reactions [69] that can alter local atomic ordering [70]. Moreover, due to the high equipment cost, the cost of preparing a TEM specimen by FIB is relatively high [71].

2. Strain analysis

To satisfy Moore's law, electronic semiconductor devices require halfing their lengths every 18-24 months, so understanding their internal structure and strain has become crucial. TEM is one of the most suitable instruments to characterize the local strain. Many TEM techniques can be applied to measure local strain fields and can be divided into 3 groups: a) based on lattice image analysis, HRTEM images/HR-HAADF-STEM images can be processed to form strain maps that can be analyzed by using geometrical phase analysis (GPA) [72], b) based on diffraction analysis, strain maps can be formed by using NBED [53], precession electron diffraction (PED) [73], CBED [54] or 4D-STEM techniques [74], c) based on phase shift measurements of the electron waves, holograms can be used to determine the deformation of the specimen, especially using dark field electron holography (DFEH) [75].

Accepted Manuscript

2.1 Strain mapping from atomic-resolution images

Strain mapping assumes a perfect 1:1 correspondence between dots in a lattice image and the positions of the underlying atomic columns so expansion/contraction of the first can be interpreted as tensile/compressive strain in the latter. It was originally developed for lattice defects in homogeneous materials for which this can be guaranteed [72], however, its use has since often been extended to interfaces between different materials where this is no longer necessarily ascertained, in particular:

a) For cubic materials, such as sphalerite or elemental semiconductors, imaging along a <100> zone axis preserves the double mirror symmetry of the structure in this projection so that atomic columns should appear either always bright or always dark so dots are located exactly on top of atomic column sites or exactly in-between [76]. In case of beam tilt, the whole pattern can move, but in the same way for all materials either side of an interface. Along the much more commonly used <110> zone axis, however, the dumb-bell like images of the projected sphalerite structure are no longer mirror-symmetric (as one column is occupied by group III atoms, the other by group V atoms) so that the extrema of the dot pattern can freely move along the dumb-bell axis without any fixed relationship with the underlying atomic columns. This makes the analysis of single mono- or bi-layer distances unreliable for sharp interfaces and should be avoided for zincblende type materials [77].

b) Measuring dot positions works best when their form does not change, i.e. if there is no visible contrast difference in the materials either side of an interface or boundary. Defoci and thicknesses of pronounced contrast changes should thus be avoided, in particular for the case of sphalerite structures imaged along <110> where even small focus changes can make the dumb-bell structures observed contract or expand [78], whether dumb-bell contrast is resolved or not.

Hÿtch et al [72]. proposed the GPA method in 1998, providing an effective tool for quantitatively measuring strain through high-quality HRTEM images. Strain induces phase changes in electron diffraction contrast images. GPA reconstructs strain information within the crystal by calculating the phase differences between adjacent pixels in the lattice image. A more widely used method is to map the strain field by measuring the local displacement of lattice fringes and assuming that these lattice fringes coincide with the positions of the underlying atomic columns. HRTEM

Accepted Manuscript

1
2
3
4
5
6
7
8
9
10
11
12
13
14
15
16
17
18
19
20
21
22
23
24
25
26
27
28
29
30
31
32
33
34
35
36
37
38
39
40
41
42
43
44
45
46
47
48
49
50
51
52
53
54
55
56
57
58
59
60

utilizes transmitted electrons for imaging, and during the transmission process, phase shifts occur due to collisions and scattering. So far, the GPA method has successfully been applied to study strain fields in quantum dots [79], nanowires [80], dislocations [81], and interfaces [82]. This integrated approach offers a robust means of gaining in-depth insights into the stress and strain behaviour of materials.

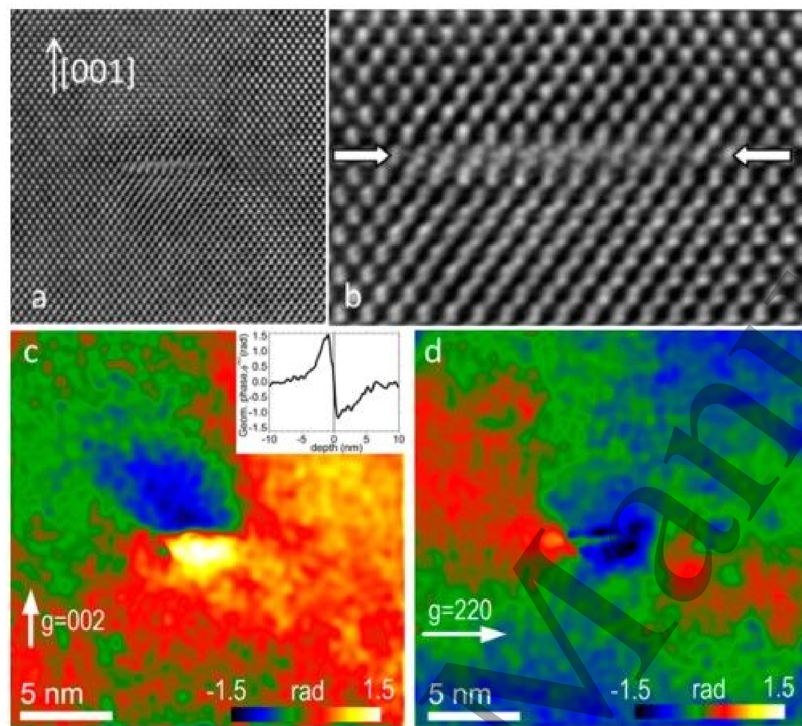

Fig. 3. GPA of a dislocation loop in a boron implanted silicon sample annealed by a single laser pulse at 2.6 J/cm^2. (a) HRTEM image in [-110] orientation,Scale bar in the inset is 5 nm; (b) enlarged view of the dislocation. The habit plane is (001),Scale bar in the inset is 1 nm; (c) geometric phase image of the 002 lattice fringes from (a) with insert of vertical displacement profile across the centre; (d) geometric phase image of the 220 lattice fringes from (a) [83].

In their study of the evolution of structural damage and dopant distribution during laser thermal annealing of ion-implanted silicon, Qiu and colleagues applied GPA to HRTEM images of the annealed samples, which allowed the observation of (001) dislocation loop defect formation (Figure 3). Figure 3a shows the HRTEM images of an area containing a loop seen edge-on, and Figure 3b shows the enlarged image of the defect itself. After Fourier transform of the original HRTEM image, the phase images P_{002} and P_{220} of the 002 and 220 Fourier spots, corresponding to the displacement of the corresponding lattice fringes, are calculated, and shown in Figures 3c and

Accepted Manuscript

1
2
3
4
5
6
7
8
9
10
11
12
13
14
15
16
17
18
19
20
21
22
23
24
25
26
27
28
29
30
31
32
33
34
35
36
37
38
39
40
41
42
43
44
45
46
47
48
49
50
51
52
53
54
55
56
57
58
59
60

d, respectively. By extracting phase images, a clear vertical dipole can be seen in the P_{002} image. The results are explained in terms of the modification of the defect formation energy induced by the compressive biaxial stress developed in the non-melted regions during laser annealing [83].

However, its applicability is constrained by certain limitations. Firstly, HRTEM has stringent sample requirements, as any thickness variation could lead to contrast reversal artifacts, i.e. thin specimens often necessitate preparation without thickness variation in the field of view. Additionally, several studies suggest that the thinning process required for preparing TEM samples may result in strain relaxation due to the high surface-to-volume ratio after the thinning process [84]. Ensuring an adequate thickness of TEM samples is crucial for obtaining meaningful and accurate strain measurements [84]. Furthermore, HRTEM images have a very small field of view, confined to the nanoscale. As a result, this method can only analyze local stresses and strains at nanometer scale, limiting the analysis of the overall sample properties. Finally, for GPA, the spatial resolution is fundamentally limited by the use of a mask selecting the Bragg spots in the Fourier space of the HRTEM image. In a semiconductor, this corresponds to typically about 0.6 nm when (002) planes are analyzed [85].

Advanced TEM instruments offer a stable bright electron source. With a spherical aberration corrector, a small electron probe can be formed so atomic column resolved HAADF images in STEM mode can be formed. GPA can also be applied to HR-HAADF images. HR-HAADF images are generated by collecting signals from electrons scattered through wide angles [86],[87]. The HR-HAADF image is very sensitive to atomic numbers, directly detecting heavy elements in materials, achieving sub-angstrom spatial resolution [88]-[90].

Accepted Manuscript

1
2
3
4
5
6
7
8
9
10
11
12
13
14
15
16
17
18
19
20
21
22
23
24
25
26
27
28
29
30
31
32
33
34
35
36
37
38
39
40
41
42
43
44
45
46
47
48
49
50
51
52
53
54
55
56
57
58
59
60

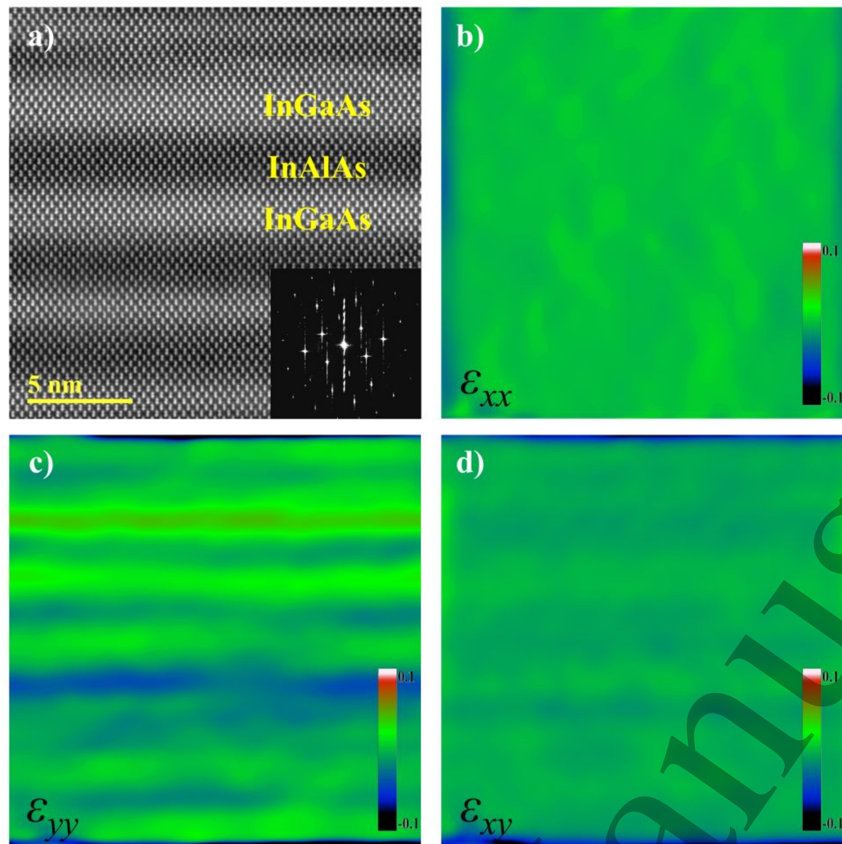

Fig.4. a) High-resolution HAADF shows the atomic structure of a quantum well (QW) in a quantum cascade laser device, where InGaAs layers appear bright. b)-d) correspond to the strain distributions in [*xx]*, [*yy]* and [*xy]* directions. The mean strain (2.27×10^{-5}) in *xx* direction [110] is much less than the mean strain (2.72×10^{-3}) in [*yy]* direction [002], which means the strain in the interface accounts for most of the strain in this layer structure.

In figure 4, the HR-HAADF-STEM images, combined with the GPA method, were employed to investigate and understand the strain induced by the quantum well (QW) in the quantum cascade laser device. By examining the strain in various directions, we can infer that the interlayer strain contributes significantly to the overall strain within the layered structure. As ion milling is necessary for producing the electron transparent region of TEM samples, the effective ion bombardment could lead to an apparent change of internal strain, which prevents precision strain measurement. Therefore, a comparative analysis should be carried out by non-destructive integral X-ray diffraction (XRD) mapping, which can act as a reference for ensuring the accuracy of the local TEM measurement [91]-[93].

Compared to HRTEM, HR-HAADF-STEM is less sensitive to the sample thickness and thickness

Accepted Manuscript

1 2 3 4 5 6 7 8 9 10 11 12 13 14 15 16 17 18 19 20 21 22 23 24 25 26 27 28 29 30 31 32 33 34 35 36 37 38 39 40 41 42 43 44 45 46 47 48 49 50 51 52 53 54 55 56 57 58 59 60

variation, i.e. less sensitive to TEM sample preparation [94]. In addition, as the image is formed by collecting the signals during rastering of the ROI, the field of view can be as large as a few hundreds of nanometers compared to the nanometer scale image recorded by HRTEM. However, the precision of the strain maps is usually not as high as those of maps generated through DP or holography [95]. Therefore, the strain maps generated by using GPA through HR-HAADF-STEM images are mainly useful for quickly examining large deformations in the specimen due to relatively large changes in strain, with precision around 0.2-0.4% [94] in the lattice parameter.

2.2 Electron Diffraction

Both near-parallel electron beams with small convergence angles and large-angle convergent electron beams can result in DPs, corresponding respectively to NBED and CBED. Diffraction spots, which are directly related to the atomic distances, are formed by using the parallel or near-parallel beam to illuminate the specimen; on the other hand, diffraction discs can be formed by a convergent electron beam. NBED and CBED are electron diffraction techniques that evolve with an increasing convergence angle of the incident electron beam [96],[97] (Figure 5). According to Bragg's law, the incident electrons will be deflected by the crystal lattice, generating diffraction patterns [98]. The resulting diffraction patterns exhibit variations due to distinct crystal structures. By analyzing these diffraction patterns, internal strains within the crystal can be reconstructed with very high sensitivity.

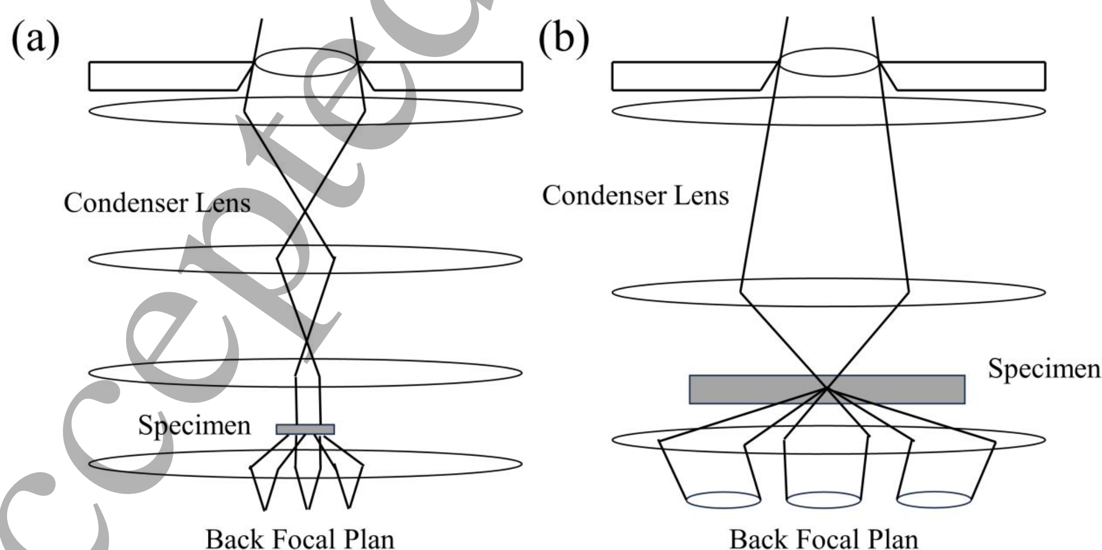

Fig. 5. (a) Nanobeam electron diffraction mode; (b) convergent beam electron diffraction mode.

Accepted Manuscript

NBED uses a near-parallel beam with a small convergence angle to scan the ROI, recording the DP at each point. The diameter of the probe formed by a near-parallel beam can reach sub-10 nm by using a small condenser aperture (diameter < 20 μm), which defines the spatial resolution of this method. NBED obtains information on the crystal structure by performing reciprocal space analysis of the pattern obtained from electron diffraction [99]-[101]. Strain can be calculated by comparing the diffraction pattern obtained from the ROI with that obtained from a reference, non-strained region. These measurements are useful in studying the stress state, dislocation generation, and propagation mechanisms in epitaxial semiconductor materials [102]-[104].

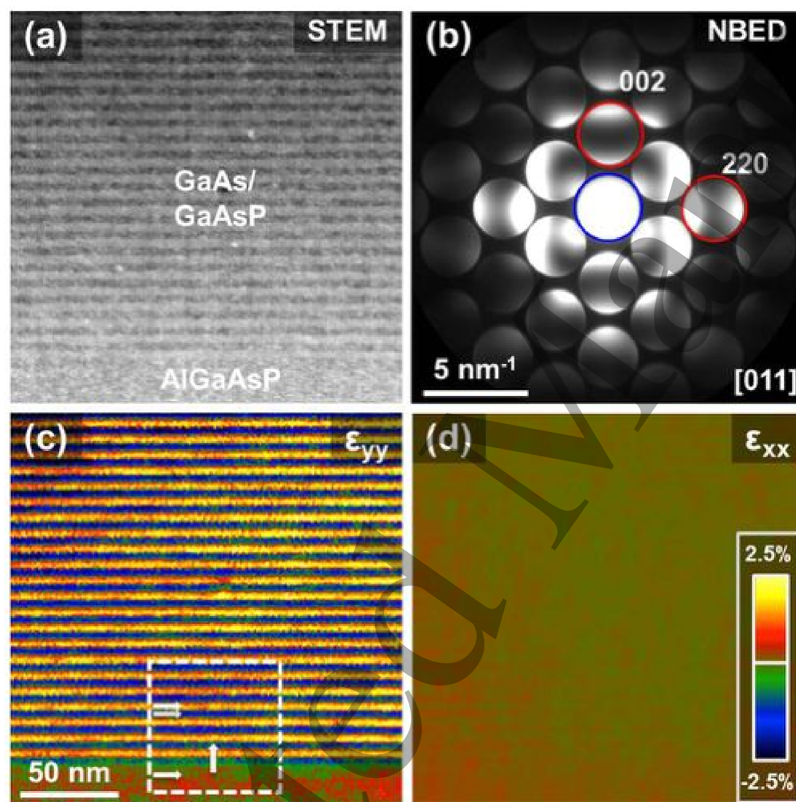

Fig. 6. NBED analysis of a GaAs/GaAsP multilayer device in cross-section. (a) HAADF image of the analyzed section. (b) Representative nano DP taken from the dataset, with the 002 and 220 diffraction vectors that were analyzed for the strain analysis highlighted. (c) NBED strain map of strain along y = [002] direction. (d) NBED strain map of strain along x = [220] direction [105].

Ozdol et al. [105] combined the NBED technique with a fast electron detector to improve its sensitivity. By applying this method to map the strain contour of GaAs/GaAsP superlattice (SL)

Accepted Manuscript

1
2
3
4
5
6
7
8
9
10
11
12
13
14
15
16
17
18
19
20
21
22
23
24
25
26
27
28
29
30
31
32
33
34
35
36
37
38
39
40
41
42
43
44
45
46
47
48
49
50
51
52
53
54
55
56
57
58
59
60

structures, they demonstrated that the combination of these two techniques had excellent characterization capabilities for high-quality heterostructures and low-defect regions (Figure 6), which confirms the NBED technique is well-suited for high-precision, high spatial resolution, and large field-of-view strain characterization.

The problem with NBED is the potential saturation of the detector during over-exposure, therefore it is difficult to determine the peak position of each diffraction spot. This issue is effectively addressed by PED [106],[107]. PED was initially referred to as the double-cone beam-rocking method [108] where the incident electron probe is tilted by an angle φ off the optic axis and rotates azimuthally around the axis, illuminating the sample like a cone-shaped beam. The tilted electron beam extends the zero-order Laue zone from a point to a ring, effectively collecting diffraction information from different directions around the optic axis. As a result, PED provides more accurate crystallographic information with less influence from dynamical scattering [109]. PED has been proven beneficial for orientation imaging [110]-[112], phase identification [113], strain mapping [114]-[116] and three-dimensional phase crystallography [117]. ABashir et al. [118] utilized PED technology to measure the cross-sectional strain field of a Ge micro-disk under tensile strain induced by Si_3N_4 stressors. The strain maps were interpreted and compared with finite element models of the studied structure, demonstrating excellent consistency. This highlights the applicability of PED technology to strain mapping. Simultaneously, the study revealed that this technique also allows the observation of strain relaxation caused by dislocation pile-ups, further substantiating the benefits of this experimental approach.

CBED is a dynamic diffraction-based method that can distinguish between polar and non-polar crystals [119],[120]. It allows for the unique identification of all point groups based on the symmetry present in the CBED discs [121],[122]. The principle of CBED involves focusing a large-angle electron beam onto the surface of a sample and selecting a small range of lattice points within the sample for electron diffraction by controlling the incident angle and direction of the electron beam. Instead of typical diffraction spots, circular diffraction discs are formed (Figure 5(b)) [123]. The intensity of the diffraction in the disc can be compared with the diffraction intensity calculated based on dynamic diffraction theory. CBED based on dynamic diffraction theory enables the determination of fine structures, such as crystal structure, orientation, lattice distortion and strain information within the material [124]-[126]. CBED focuses on the symmetry

Accepted Manuscript

1 2 3 4 5 6 7 8 9 10 11 12 13 14 15 16 17 18 19 20 21 22 23 24 25 26 27 28 29 30 31 32 33 34 35 36 37 38 39 40 41 42 43 44 45 46 47 48 49 50 51 52 53 54 55 56 57 58 59 60

and crystallography of single crystalline samples and if the sample needs to be slightly tilted, this can cause structural shadowing especially for thicker samples, therefore it may not be suitable for all specimens.

In contrast to the diffraction techniques mentioned earlier, 4D-STEM technology allows for the simultaneous acquisition of the entire electron diffraction pattern at each scan position [127],[128]. Conventional STEM detectors record a single intensity value per probe position (where BF, LA-ADF and HA-ADF detectors can be used simultaneously, giving three intensity values at each point). In 4D STEM, the probe is rastered over the specimen in a 2D array while at each probe position, a 2D diffraction pattern is imaged on a pixelated detector, which generates a 4D data cube. This full-field scanning approach empowers 4D-STEM with enhanced information acquisition capabilities, particularly demonstrating excellence in studying complex systems such as polycrystals, nanostructures, and amorphous materials, cf. for instance, the in-situ strain work conducted by Gammer et al. [129].

4D-STEM is an advanced technique employed for investigating the structural and dynamic behaviour of materials [130]. Integrating STEM with electron diffraction techniques, this technology enables the study of stress-strain characteristics in materials at the nanoscale. In recent years, 4D electron microscopy has experienced rapid development [131], attaining high temporal resolution for imaging diffraction patterns. The transient behaviour of diffraction patterns reflects lattice dynamics as non-equilibrium atomic motion induces changes in atomic displacements, influencing electron interference. By observing variations in Bragg reflections, changes in atomic distances can be elucidated. Under near-parallel electron beam illumination, the technology allows for precise detection of strain-driven unit cell distortions induced by lattice compression or expansion.

Accepted Manuscript

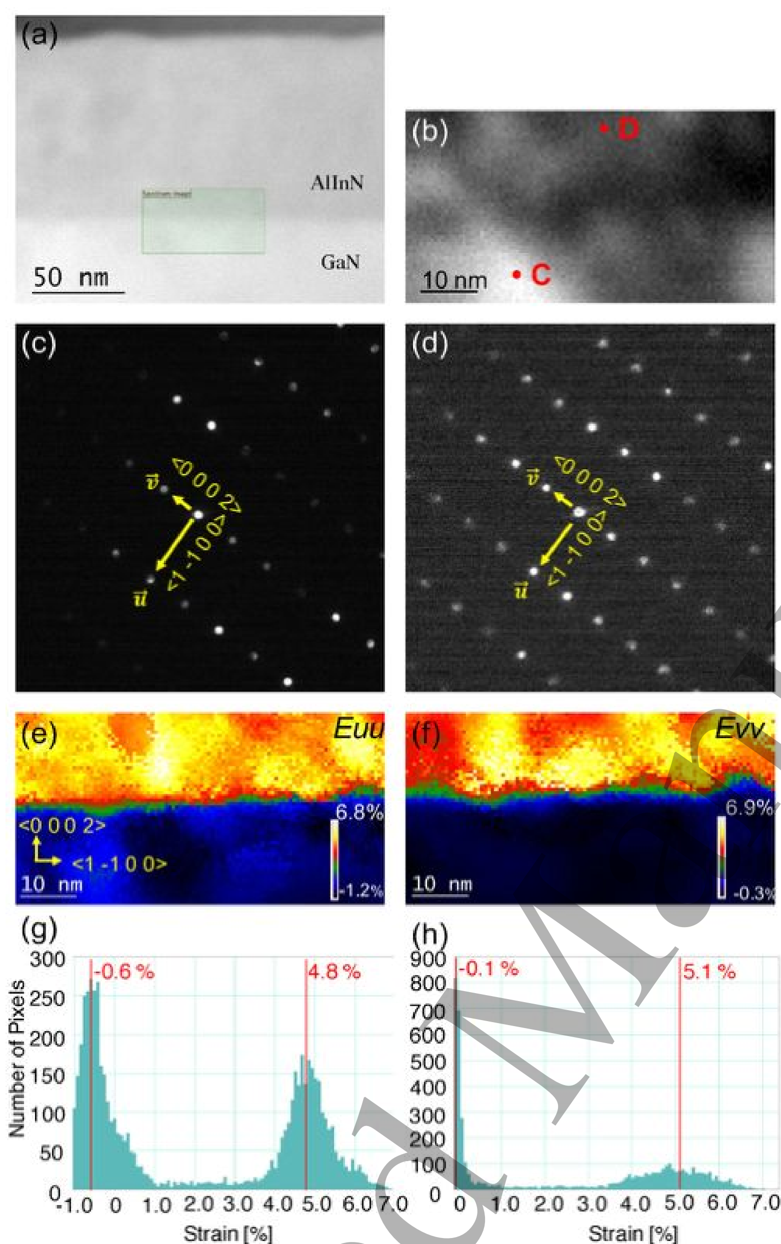

Fig.7. Strain-field map calculated from lattice expansion in 4D-STEM nano-beam diffraction patterns. (a) Dark-field STEM image close to the <11-20> pole with the rectangle showing the scanned area for 4D-STEM. (b) The scanned 4D-STEM image including the AlInN/GaN interface. (c) and (d) are diffraction patterns taken at points C and D in (b). (e) and (f) are strain maps calculated from local nanobeam diffraction patterns in (b) corresponding to *u*=[1-100] and *v*=[0002], respectively. (g) and (h) are histograms of strain vs the number of pixels of the corresponding strain map in (e) and (f), respectively [132].

Motoki et al. [132] used 4D-STEM to investigate $Al_{0.3}In_{0.7}N$ grown on GaN. They obtained images near the AlInN/GaN interface (Figures 7(a), (b)) and strain maps by analyzing the

Accepted Manuscript

1 2 3 4 5 6 7 8 9 10 11 12 13 14 15 16 17 18 19 20 21 22 23 24 25 26 27 28 29 30 31 32 33 34 35 36 37 38 39 40 41 42 43 44 45 46 47 48 49 50 51 52 53 54 55 56 57 58 59 60

movement of diffraction spots between diffraction patterns (Figures 7(e), (f)). The study revealed that interface-generated dislocations lead to sudden strain relaxation, resulting in higher-quality film growth. They concluded that compared to traditional MBE or MOVPE deposition techniques, metal modulated epitaxy (MME) would be ideal for growing high-quality indium-rich AlInN films.

Due to the high-order Laue zones (HOLZ) line broadening effect (the uncertainty in the crystal orientation distribution in polycrystalline samples due to the thermal vibrations of atoms in the lattice), CBED cannot be used for many semiconductor device samples [133],[134]. On the other hand, NBED requires a sufficiently small electron beam [74], which demands careful experimental setup and stable instrument performance. The non-uniform intensity in the diffraction spots may lead to incorrect determination of their positions [94]. PED necessitates advanced instrumentation with precise control over electron beam precession [135]. The rotation of the electron beam in PED increases the data acquisition time significantly. Prolonged exposure to the electron beam during PED can cause irreversible damage to the sample [136]. 4D-STEM has garnered considerable attention due to its high angular resolution, high spatial resolution, extensive data acquisition capabilities, and the ability to provide dynamic information about samples. However, this technique also presents certain limitations. The large amount of data generated by 4D-STEM necessitates highly complex computations and algorithms for data collection, processing and interpretation [137]. Additionally, the extended time required for experimental setup and data acquisition results in relatively lower experimental efficiency [138]. 4D-STEM is more flexible, providing a comprehensive and powerful tool for a broader range of material studies. This evolution of diffraction techniques aims to meet the growing demands in materials science for a more comprehensive and in-depth characterization of microstructure and properties, indicating new directions for the future development of electron microscopy techniques.

2.3 Electron Holography

Electron holography was invented by Gabor in 1949 as a method to extend the resolution limit of electron microscopy [75],[139]. In traditional electron micrographs, the recorded intensity represents the squared modulus of the electron wave, and the phase information of the wave is

Accepted Manuscript

Accepted Manuscript

lost. This absence of phase information implies a significant loss of object information, where the phase shift of the electron wave reflects the interaction of incident electron and material. As phase can only be detected through interferometric measurement methods, holography has found widespread application in various phase measurement techniques. Holograms can be recorded in the near field (Fresnel holography) [140], far field (Fraunhofer holography) [141], and Fourier spectrum (Fourier holography) [142]. The principle involves superimposing a reference wave onto the target wave to create an interference pattern for phase recording.

Initially, Gabor proposed in-line holography, where the reference and object waves propagate in the same direction. However, during the reconstruction process, the problem of two overlapping conjugate waves creating twin images arose, making them indistinguishable. Leith and Upatnieks [143] addressed this twin-image problem by introducing an angle θ between the reference and object waves, later separating the reconstructed twin waves at an angle of 2θ. In 1968, Möllenstedt and Wahl recorded the first off-axis Fresnel hologram and successfully reconstructed micrographs using lasers [144]. Subsequently, Wahl adapted off-axis holography from an optical perspective to develop imaging technology in electron microscopy [145]. To date, off-axis electron holography remains the most successful and widely used holographic method in electron microscopy [146]. In TEM, inserting an electron biprism allows the superimposition of the electron wave with a planar reference wave to record holograms [147]. Reconstructing the entire electron wave from holograms, electron holography enables comprehensive analysis of almost all object features at atomic resolution. Due to the sensitivity of phase shifts to local variations in magnetic fields and electrostatic potentials, electron holography can provide quantitative information about magnetic and electric fields inside materials and devices [148],[149].

Reproducible recording of holographic fringes requires a very stable instrument. The wavelengths of electrons are very short, in the picometer range, so that the fine fringes are to be recorded at extremely high magnifications and are prone to blur and noise due to drift and stray fields. Once holograms have been successfully recorded through this process, it is possible to reconstruct the three-dimensional phase information of the sample, providing detailed microscopic structural features, including lattice distortions, dislocation distributions, and strains [150]. Compared to traditional images, electron holographic images offer more comprehensive information. In modern times, advanced electron holography techniques can not only achieve real-time dynamic

1
2
3
4
5
6
7
8
9
10
11
12
13
14
15
16
17
18
19
20
21
22
23
24
25
26
27
28
29
30
31
32
33
34
35
36
37
38
39
40
41
42
43
44
45
46
47
48
49
50
51
52
53
54
55
56
57
58
59
60

observations [151] but also enable three-dimensional reconstruction of electromagnetic fields [152] and high-sensitivity phase measurements [153]. These advances underscore the growing importance of electron holography in the fields of materials science and device research.

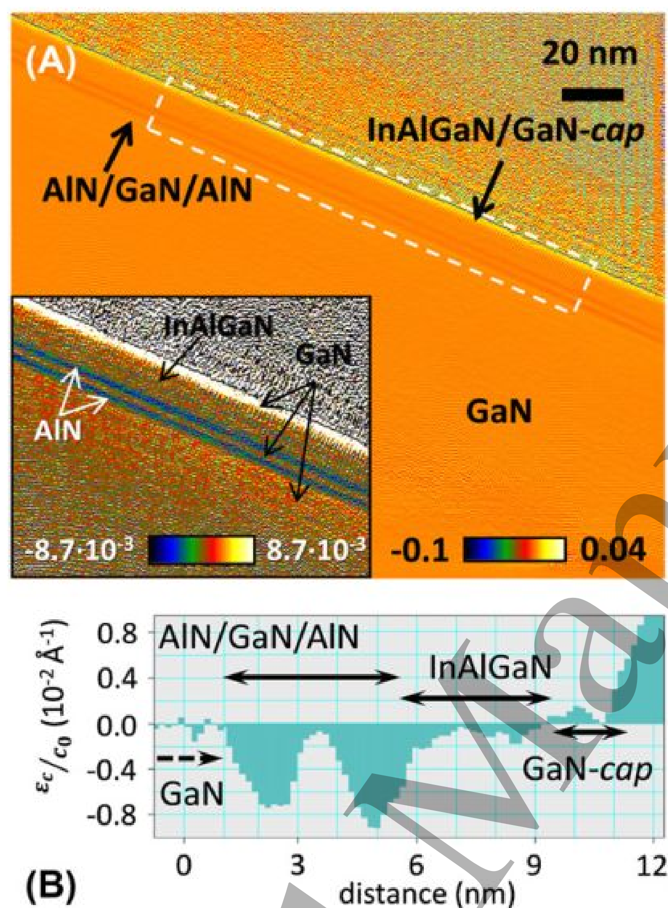

Fig. 8. (A) Normalized strain map along the growth direction. The dashed rectangle indicates the area from which the line profile (B) has been extracted. An inset is presented with another colour scale, so that the strains in different layers are easier to distinguish. (B) Averaged strain to lattice constant ratio of the top layers [154].

In the process of investigating the bandgap of III-N compounds, Manuel et al. [154] employed inline holography to obtain strain maps of InAlGaN/GaN. Utilizing the full-resolution wave reconstruction algorithm [155], they obtained normalized strain maps (Figure 8 (a)). The study revealed that biaxial strain in III-N alloys reduces the bandgap energy. In the case of lattice-matched (virtually strain-free) heterostructures, the calculated values agreed well with experimental results.

Accepted Manuscript

1
2
3
4
5
6
7
8
9
10
11
12
13
14
15
16
17
18
19
20
21
22
23
24
25
26
27
28
29
30
31
32
33
34
35
36
37
38
39
40
41
42
43
44
45
46
47
48
49
50
51
52
53
54
55
56
57
58
59
60

Electron holography technology, especially DFEH, has demonstrated immense potential in strain mapping due to its unique combination of precision (10^{-4}), good spatial resolution (4nm), and large field of view (μm^2) [156]. However, this approach still faces certain limitations. Despite utilizing reference waves from a disturbance-free vacuum region, the method struggles with distinguishing strain and thickness variations in the final image due to the different diffraction patterns generated as electrons pass through samples of varying thicknesses. When dealing with samples that exhibit uneven thickness or many defects, the application of electronic holography is constrained.

2.4 Summary of this section

Accumulation of internal stress and strain in semiconductor materials may induce defect generation within the material. When semiconductor materials experience a certain level of internal strain, the bonding between atoms undergoes changes, leading to the formation of defects, including point defects, linear defects and planar defects. These defects have a significant impact on the electrical and optical properties of the material. Additionally, internal stress may trigger microstructural changes in the material, such as crystalline phase transitions, thereby influencing the electronic transport properties and optical characteristics of the material. For instance, it can affect the migration and recombination processes of charge carriers, consequently impacting the electrical performance of devices.

Therefore, in the field of semiconductor materials research, a thorough understanding of the influence of internal stress and strain on material properties is crucial. As shown in Table 1, research on how internal stress and strain lead to defect formation contributes to a better comprehension of material characteristics, providing essential insights into material design and device manufacturing to enhance the performance and reliability of semiconductor devices.

Accepted Manuscript

1 2 3 4 5 6 7 8 9 10 11 12 13 14 15 16 17 18 19 20 21 22 23 24 25 26 27 28 29 30 31 32 33 34 35 36 37 38 39 40 41 42 43 44 45 46 47 48 49 50 51 52 53 54 55 56 57 58 59 60

Table 1 Summary of strain analysis methods

	Geometric phase analysis	Parallel beam electron diffraction	Convergent beam electron diffraction	Electron holography
Spatial resolution	≈0.5nm	≈10 nm	≈1 nm	≈4 nm
Precision	0.1%	0.06%	0.02%	0.01%
Type of information	surface	surface，inside	surface，inside	inside
Field of view	nm^2	μm^2	μm^2	μm^2
Data processing	simple	extensive	extensive	extensive
Special equipment	no	yes	yes	yes
Mapping	quick	slow	slow	intermediate
Operational difficulty	easy	medium	medium	hard

3. Defect characterization

The characterization of defects in semiconductor materials has significant importance for materials science and electronic device manufacturing. To date, researchers have identified and characterized various types of semiconductor defects, such as point defects, dislocations, grain boundaries, fractures, and segregation clusters, all of which can profoundly impact the electrical and optical properties of semiconductors. Various TEM techniques can be used to study these defects, such as weak-beam dark-field (WBDF), HAADF-STEM and BF. The comprehensive application of these characterization techniques not only advances our understanding of semiconductor defect behaviour but also provides strong support for material design and optimization of electronic device performance.

3.1 WBDF imaging under two-beam conditions

WBDF imaging is considered one of the most suitable techniques for studying dislocations and various defects and has a long history. This method employs imaging with a crystal reflection of type $\boldsymbol{g}$ when the crystal is oriented into a two-beam condition, with the Ewald sphere cutting through 0 and m$\boldsymbol{g}$, in which m is an integer. As long as $\boldsymbol{g}\cdot\boldsymbol{b} \neq 0$, a diffracted beam $\boldsymbol{g}$ can be used to

Accepted Manuscript

1
2
3
4
5
6
7
8
9
10
11
12
13
14
15
16
17
18
19
20
21
22
23
24
25
26
27
28
29
30
31
32
33
34
35
36
37
38
39
40
41
42
43
44
45
46
47
48
49
50
51
52
53
54
55
56
57
58
59
60

image dislocations with a Burgers vector ***b*** [157]. The contrast mechanism was initially explained in 1960 using kinematic diffraction theory [158], later extended by Howie and Whelan's dynamic theory [159]. In 1969, Cockayne et al. [160] developed the WBDF technique, enabling defects to be imaged with sufficient spatial resolution, distinguishing individual partial dislocations with an approximate separation of 10 nm. In crystals, the lattice distortion around defects causes a change in the scattering intensity. When the change in scattering intensity caused by defects is subtle, it cannot be directly observed, and weak-beam conditions enhance the detection and imaging of these weak scattering signals. By adjusting lenses or gratings in the microscope, specific diffraction points exhibiting a change in scattering intensity are selectively observed, highlighting weak scattering signals caused by defects or local strains [161],[162]. The formation of WBDF-TEM images is based on the two-beam condition. The main processes include [163] the following steps: a) adjusting the sample orientation to achieve the two-beam diffraction condition, exciting only the direct beam and one diffraction vector ***g***; b) tilting the electron beam to tilt the reflected ***g*** toward the optical axis, known as the ***g*** (3***g***) condition when 3***g*** lies on the Ewald sphere while ***g*** is away from the Ewald sphere, introducing a significant positive excitation error; c) inserting the objective aperture, selecting the central reflection ***g*** to obtain WBDF-TEM images. WBDF imaging utilizes a larger excitation error (***s***) for the selected diffraction vector ***g***, as the width of dislocations is related to the excitation distance, resulting in a smaller effective excitation distance and narrower images of most defects. This technique provides a high-resolution means for studying dislocation microstructures [164],[165].

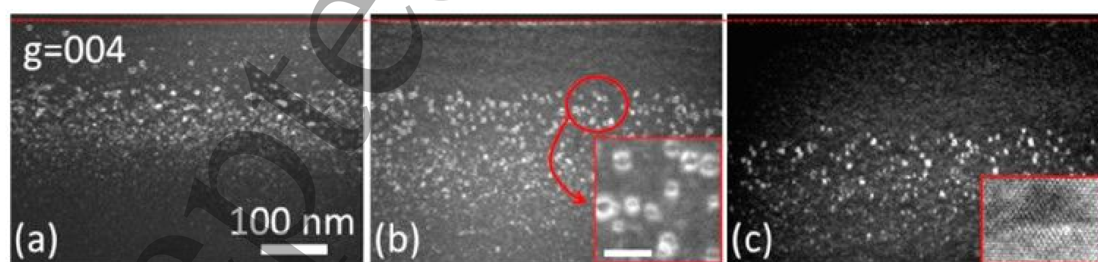

Fig.9. Cross-sectional WBDF TEM images (surfaces are indicated by the red dashed line) of a silicon implanted sample annealed by (a) 10 pulses at 1.5 J/cm^2 (non-melted), (b) 1 pulse at 2.6 J/cm^2 (partially melted above R_p). Scale bar in the inset is 20 nm, (c) 1 pulse at 2.9 J/cm^2 (partially melted below R_p). Inset: HREM image of a loop with (001) habit plane [83].

Accepted Manuscript

1 2 3 4 5 6 7 8 9 10 11 12 13 14 15 16 17 18 19 20 21 22 23 24 25 26 27 28 29 30 31 32 33 34 35 36 37 38 39 40 41 42 43 44 45 46 47 48 49 50 51 52 53 54 55 56 57 58 59 60

In their research, Qiu et al. utilized WBDF images taken with a vector of ***g***= [004] to compare non-melted, partially melted, and fully melted Si^+ ion-implanted samples under different laser annealing conditions (Figure 9). The results indicate that the positions of defects are directly correlated with the laser melting/non-melting conditions [83]. Wu et al. [166], in their investigation of the enhanced internal quantum efficiency (IQE) in step-graded GaN/AlGaN multiple quantum wells (MQWs), utilized WBDF imaging to obtain dislocation maps of the active region of the samples. The results indicated that the dislocation density was similar across all samples, and the significant differences in IQE could not be attributed to variations in defect-related non-radiative recombination rates.

WBDF imaging, renowned for its high spatial resolution in defect visualization, encounters notable limitations. The technique's reliance on specific crystallographic conditions, crucial for achieving double diffraction or two-beam conditions, imposes constraints on its adaptability across diverse crystal structures. This limitation becomes particularly pronounced when studying materials with varied defect types or orientations. Furthermore, WBDF's sensitivity to specific diffraction vectors and the associated large excitation errors confines defect imaging to those in alignment with the chosen diffraction conditions. This constraint poses challenges when investigating complex materials with a broad spectrum of different defect orientations and types.

3.2 HAADF-STEM

HAADF-STEM, also known as *Z*-contrast imaging, utilizes an annular detector to collect high-angle scattered electrons for image generation [167]-[170]. A scanning transmission electron microscope obtains a focused probe through strong co-excitation of condenser and objective lenses, causing the electron beam to form an X-shaped cross-over in the specimen plane. The beam is then deflected and scanned pointwise across the specimen surface in a raster pattern, collecting scattered intensities at each point. A ring-shaped detector integrates the intensity of transverse scattering over a large angular range, resulting in an annular dark-field image. HAADF achieves sub-Ångstrom spatial resolution, enabling atomic imaging [171]-[173].

Z-contrast can be interpreted qualitatively or quantitatively. For the latter, the exponent n in the relationship $I=cZ^n$ between intensity I and atomic number Z (where c is some constant) lies somewhere in the range n=1.2,…,2 where n=2 would describe ideal Rutherford scattering and c

Accepted Manuscript

1 2 3 4 5 6 7 8 9 10 11 12 13 14 15 16 17 18 19 20 21 22 23 24 25 26 27 28 29 30 31 32 33 34 35 36 37 38 39 40 41 42 43 44 45 46 47 48 49 50 51 52 53 54 55 56 57 58 59 60

depends on specimen thickness as well as detector sensitivity. There are several approaches to quantify this across hetero-interfaces, all of which assume that there are no abrupt thickness gradients at the interface. In terms of decreasing reliability these comprise:

a) detailed comparison with modelling taking into account phonon scattering at specimen temperature, material type, specimen thickness and orientation as well as collection angle, all of which need to be measured [174];

b) measurement of intensity I as function of camera length and extrapolation to zero camera length (corresponding to infinite scattering angle where n=2) [175];

c) comparison with dynamic elastic and frozen phonon scattering approximations [176];

d) kinematic approximative comparison using an effective value of n and an effective value of average atomic number $\langle Z \rangle$ [177];

e) calculation of the square-root of the intensity, $\sqrt{I}$, which is a better measure almost linear in $\langle Z \rangle$, before line profile analysis [178].

A particular problem with semiconductors is that many are prone to surface oxidation so that measuring and interpreting the Z-contrast of very thin specimens is not the ideal solution as here such surface oxides will make the largest relative contribution, generally reducing the image contrast. It may therefore be better to measure the ADF contrast in medium-thick samples or, even better, as function of specimen thickness [179].

Accepted Manuscript

1 2 3 4 5 6 7 8 9 10 11 12 13 14 15 16 17 18 19 20 21 22 23 24 25 26 27 28 29 30 31 32 33 34 35 36 37 38 39 40 41 42 43 44 45 46 47 48 49 50 51 52 53 54 55 56 57 58 59 60

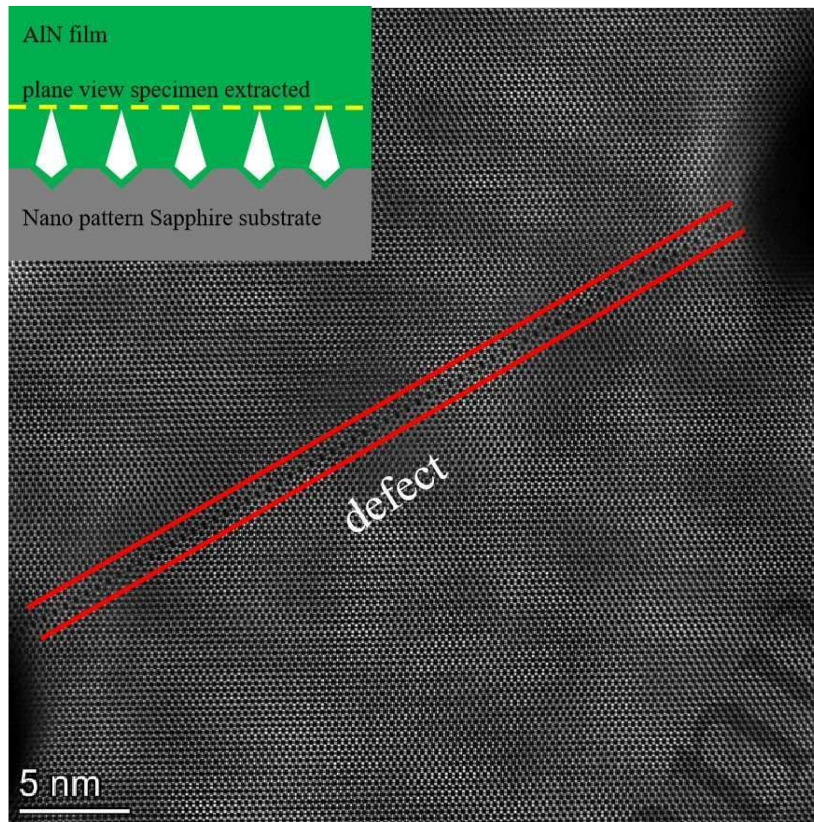

Fig. 10. HAADF image showing the atomic arrangement of stacking fault viewed along [11-20] direction. The inserted image shows the location where the specimen was taken.

Aluminium nitride (AlN) as a crucial wide-bandgap semiconductor material that exhibits exceptional properties, including a wide bandgap, high thermal conductivity and a thermal expansion coefficient compatible with III-V compound semiconductors [180]-[183]. Due to these outstanding characteristics, AlN finds extensive applications in the semiconductor and optoelectronic device manufacturing sectors, particularly in enhancing the performance of devices such as LEDs, lasers, and power electronic components. As shown in Figure 10, an AlN thin film is grown on a sapphire substrate that has undergone prior nano-patterning [184]-[186]. The yellow dashed line in Figure 10 corresponds to the region of extracted plane-view sample. The HAADF image reveals the atomic arrangement of the defect within the AlN film. The presence of the defect can impact the electrical and optical properties of the AlN film. It could result in reduced efficiency and performance in optoelectronic devices like LEDs and lasers [187]-[190].

Understanding interfaces is crucial for the study of semiconductor materials as they directly influence the mechanical, optical, compositional, chemical, and electronic properties at the atomic

Accepted Manuscript

1
2
3
4
5
6
7
8
9
10
11
12
13
14
15
16
17
18
19
20
21
22
23
24
25
26
27
28
29
30
31
32
33
34
35
36
37
38
39
40
41
42
43
44
45
46
47
48
49
50
51
52
53
54
55
56
57
58
59
60

scale. Fourier filtering of Fast Fourier Transform (FFT) patterns obtained from High-Resolution (S)TEM images is a common method used to analyze the coherence of materials interfaces [191]. The paraboloid method (PM), proposed by Van Dyck and based on Schiske's Wiener filter method [192], achieves phase correction of individual Fourier components in reciprocal space [193]. Kawasaki et al. [194] used a 3D Fourier filtering approach for wave field recovery. Filtering FFT patterns can enhance coherent structures, and if non-coherent defects like misfit dislocations are present, these manifest as distinct features at the interface. When the thickness of an interface is less than the critical thickness, Fourier filtering accurately reveals the coherence or non-coherence of the interface. However, when the thickness approaches or surpasses the critical thickness, the interface near the critical thickness exhibits diffuse blurring diffraction spots, making accurate analysis impossible. For interface thicknesses beyond the critical thickness, Matthews and Blakeslee developed analytical models based on thermodynamic assumptions and elasticity theory, and methods such as curvature measurements can be used to study misfit dislocations that occur during epitaxial growth [195],[196].

While HAADF-STEM imaging offers numerous advantages in materials research, it is not without its drawbacks and limitations. HAADF images cannot determine the elemental species, and the atomic sensitivity is relatively low for light elements or materials with low atomic numbers. In some regions with lower brightness or fine structures, it may not provide sufficient contrast and clarity. In addition, atomic column resolved HR-HAADF imaging limits the field of view. Moreover, HAADF imaging is limited to uniformly thin samples. According to the theory proposed by Pennycook et al. [170], for thicker samples such as bulk materials or thick films, multiple scattering effects may occur, leading sometimes to a noticeable degradation in image quality.

3.3 BF imaging

BF imaging is a conventional TEM microscopy technique that utilizes the intensity differences of electrons transmitted in different sample areas to reveal material structures and compositional information [197]-[199]. BF imaging is primarily employed in the morphological characterization and analysis of semiconductors, enabling direct observation of material morphology, interface information, and defects. By adjusting the conditions of the transmitted electron beam, such as

Accepted Manuscript

1
2
3
4
5
6
7
8
9
10
11
12
13
14
15
16
17
18
19
20
21
22
23
24
25
26
27
28
29
30
31
32
33
34
35
36
37
38
39
40
41
42
43
44
45
46
47
48
49
50
51
52
53
54
55
56
57
58
59
60

contrast and focus, BF imaging can provide information on the morphology, roughness, surface features, defects, dislocations, grain boundaries, and twinning of materials. Additionally, BF imaging enables clear observation of the interface status and atomic distribution between different materials, thereby assisting researchers in evaluating material quality and performance and optimizing fabrication processes [200],[201].

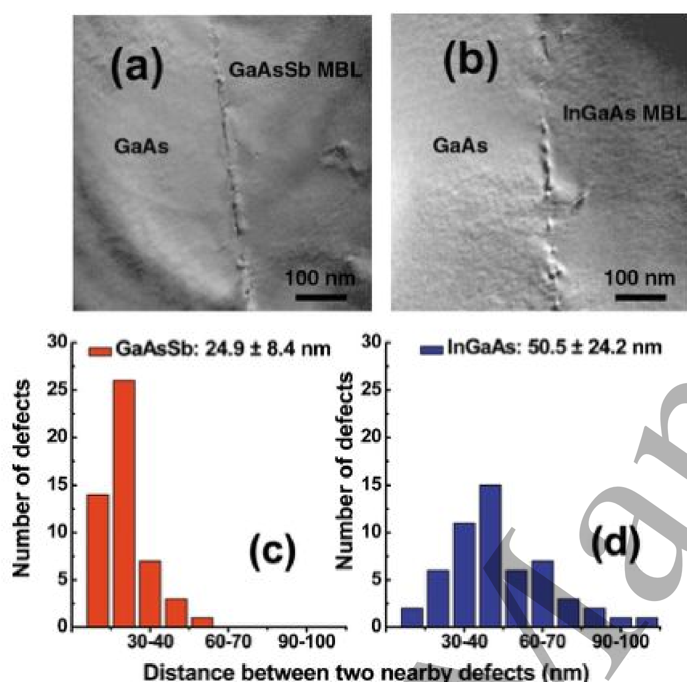

Fig. 11. Bright-field TEM images of the interfaces between (a) GaAsSb metamorphic buffer layers (MBL) and GaAs, and (b) InGaAs MBL and GaAs. The number of dislocations as a function of their spacing is shown for (c) GaAsSb/GaAs and (d) InGaAs/GaAs, respectively [202].

In the study by Liu et al. [202] on the impact of indium composition on the optical and structural properties of InAs/GaAs quantum dots in InGaAs metamorphic buffer layers (MBLs), it was found that the rough surface morphology of the buffer layer was the main cause of the decreased optical performance. In contrast, GaAsSb MBLs exhibited a smoother surface morphology, leading to an enhancement in the quantum dots' photoluminescence (PL) intensity. As shown in Figure 11, compared to InGaAs, the interface dislocations between GaAsSb MBL and GaAs result in a higher degree of strain relaxation, thereby leading to a smoother surface of the GaAsSb buffer layer.

BF images can thus provide morphological information with large field of view of the sample,

Accepted Manuscript

1
2
3
4
5
6
7
8
9
10
11
12
13
14
15
16
17
18
19
20
21
22
23
24
25
26
27
28
29
30
31
32
33
34
35
36
37
38
39
40
41
42
43
44
45
46
47
48
49
50
51
52
53
54
55
56
57
58
59
60

giving statistically meaningful information such as on the average distance between defects, with limited capabilities for analyzing the types or the crystal structures of the defects.

3.4 Summary of this section

In the characterization of nanoscale semiconductor materials and devices, conducting analyses through multiple imaging methods for the same sample is indispensable. As shown in Table 2, despite certain drawbacks associated with each electron microscopy characterization technique, combining various analytical approaches can compensate for the limitations of individual methods, enabling a more comprehensive and accurate material characterization. WBDF images can provide the Burgers vector of the defect, HR-HAADF images can provide the atomic arrangement within a single defect, while BF images can provide statistical information on morphology and defect distribution.

Table 2 Summary of defect characterization

	Weak-beam dark-field	High-angle annular dark field	Bright-field
Spatial resolution	1 nm	0.1nm	0.3nm
Precision	0.01%	0.3%	0.5%
Field of view	μm^2	μm^2	μm^2
Operational difficulty	hard	easy	easy
Atom sensitivity	no	heavy atoms	light atoms

4. **Evaluation of bandgap by VEELS**

The concentration and energy distribution of charge carriers in a semiconductor is given by the density of states, which describes the number of quantum states that are available per energy interval and volume in a system. Valence electron energy-loss spectroscopy (VEELS) is a specific method in EELS where a high energy electron is inelastically scattered by (bound) valence electrons. VEELS can serve as a powerful technique for investigating the bandgap by directly probing the joint density of states [203], where the probe size, fine spectral structure and energy onset of the JDOS can be used to reveal the electronic transition at nanometer scale.

Accepted Manuscript

1
2
3
4
5
6
7
8
9
10
11
12
13
14
15
16
17
18
19
20
21
22
23
24
25
26
27
28
29
30
31
32
33
34
35
36
37
38
39
40
41
42
43
44
45
46
47
48
49
50
51
52
53
54
55
56
57
58
59
60

The use of bandgap measurements by VEELS technique has been hindered by the limited energy resolution of electron source as well as the delocalization of the inelastic scattering event in the low energy-loss regime. Schottky field-emission sources typically yield energy resolution defined as the full width at half maximum (FWHM) in the range of 0.6-1.2 eV, but the asymmetry in the zero-loss peak caused by the emission process itself complicates data extraction in the low-energy loss regime, impacting the accurate determination of band-edge onset below 5 eV [204]. On the other hand, cold field emitters can give 0.3-0.6eV FWHM but have a long tail on the other side due to the Fowler-Nordheim distribution, so this only helps marginally. For semiconductors with bandgap energy lower than ~5 eV [205], VEELS studies conducted on transmission electron microscopes equipped with a cold field emission electron source can achieve an energy resolution as low as 0.3 eV [206]. TEMs equipped with an electron monochromator [207],[208] and a high-resolution electron energy-loss spectrometer [209] allow energy resolution better than 0.1 eV [210]. The recording of fine structures of JDOS enables the direct correlation of EELS with density function theory (DFT) simulations [211].

Currently, there are several approaches for obtaining the bandgap energy [212]-[215]: the first method involves directly reading off the energy of the intensity rise after the first minimum without performing zero-loss peak (ZLP) subtraction. However, due to the background intensity of ZLP, the starting point of the actually measured spectral peak may precede the onset of the bandgap [216]. Therefore, this direct reading method is considered an unreliable approach for measuring material bandgaps. The second method involves the deconvolution of zero-loss peak to obtain the single-scattering distribution, where a subsequent Kramers-Kronig analysis is expected to give a good estimation of bandgap energy and dielectric function [217]. Of note, for probing semiconductors with sufficient large dielectric constant, the presence of Cherenkov loss can compromise an accurate measurement of bandgap [218],[219]. Therefore, in order to obtain the bandgap with an excellent precision, either a low accelerating voltage or a small collection angle should be used to eliminate the influence of Cherenkov radiation [220]. Detecting and measuring where the low-loss EELS intensity increases in practice is made difficult by various other factors than can contribute intensity in the low-loss regime, such as

a) extended zero-loss tails from the emitter (stronger for a narrow cold field emitter than for a broader thermionic emitter [220] and really only eliminated by a monochromator! [221]),

Accepted Manuscript

1
2
3
4
5
6
7
8
9
10
11
12
13
14
15
16
17
18
19
20
21
22
23
24
25
26
27
28
29
30
31
32
33
34
35
36
37
38
39
40
41
42
43
44
45
46
47
48
49
50
51
52
53
54
55
56
57
58
59
60

b) intra-band scattering [222],

c) Cherenkov radiation [228],

d) low-energy surface plasmons [223],

e) volume plasmons that extend down into the bandgap region [224].

The onset for direct bandgap transitions is always more easily to detect than for indirect bandgaps. Generally, the energy resolution measured as FWHM has got no relationship at all with the reliability of a bandgap measurement, which will much more depend on how background intensity has been subtracted, whether deconvolution has been applied and over what energy range the fitting of a JDOS model was applied [22]. Narrow fit ranges can only be used to compare VEELS of the same material measured in the same set-up as function of external parameters such as temperature, pressure, doping etc. that do not significantly alter the JDOS but this should generally be avoided [225] if bandgaps are to be measured reliably and compared between different materials.

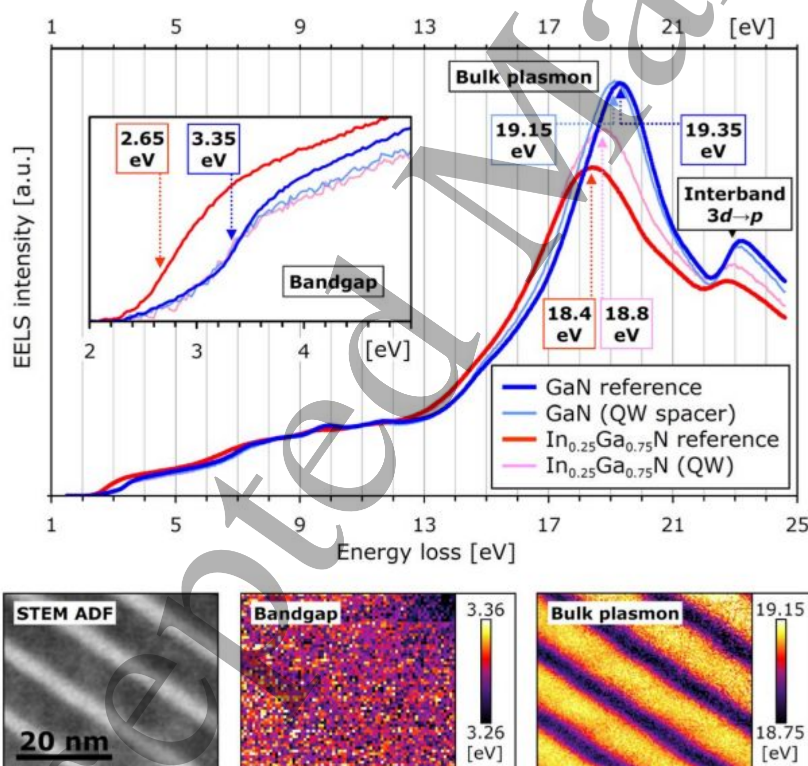

Fig. 12. Low-loss EELS spectra taken from the central 1.5 nm of an $In_{0.25}Ga_{0.75}N$ quantum well (pink) and from the GaN spacers between the quantum wells (light blue), compared with bulk $In_{0.25}Ga_{0.75}N$ (red) and GaN reference spectra (dark blue). The spectrum inset shows a close-up of

Accepted Manuscript

the bandgap features. The lower part of the figure shows a STEM ADF image, taken with the same probe settings as the adjacent EELS maps, a map of the bandgap energy (binned twice) and the bulk plasmon energy of the four quantum wells [226].

As an example, Bosman et al. [226] explored the bandgap energy of InGaN compounds using monochromatic VEELS. As shown in Figure 12, the technique has proven to be useful for correlating the chemical composition and bandgap energy. In addition, it is necessary to consider the delocalization of inelastic scattering. At lower energy ranges, the spatial resolution is poor, leading to averaging issues in the test results. Corresponding computational transformations are required to obtain accurate results [63]. The relationship between local chemistry and bandgap energy allows the user to investigate chemistry induced bandgap variations at the nanometer scale, for example, the quantification of phase separation and its related bandgap distribution in high In content InGaN ternary alloys [227].

The VEELS technique introduces possible bandgap measurements at nanometer scale. As shown in Table 3, VEELS has many advantages over conventional luminescence methods, however, challenges arise due to factors such as ZLP peak tails, spectral resolution of the (non-) monochromatic instrument and Cherenkov radiation [228] both of which will affect the precision of bandgap determination. Therefore, it is necessary to optimize the probe monochromation and accelerating voltage, which allows high quality VEELS data for signal processing.

Table 3 Comparison of bandgap measurement methods

	Valence electron energy loss spectroscopy	Cathodoluminescence
Energy resolution	0.1eV	<0.01eV
Type of information	inside	surface
Data processing	hard	easy
Special equipment	electron energy filter	optical spectrometer
Mapping	quick	quick
Operational difficulty	hard	easy
Spectral background signal	strong	weak but possible artefacts from higher diffraction orders

Accepted Manuscript

1 2 3 4 5 6 7 8 9 10 11 12 13 14 15 16 17 18 19 20 21 22 23 24 25 26 27 28 29 30 31 32 33 34 35 36 37 38 39 40 41 42 43 44 45 46 47 48 49 50 51 52 53 54 55 56 57 58 59 60

5. **In-situ TEM techniques**

In-operando techniques are a means of studying the behaviour and performance of materials in-situ [229]-[232]. The fundamental principle of in-operando techniques lies in providing the actual operation conditions while measuring and observing materials in the microscope, to acquire time-resolved information on important processes such as structural changes, phase transitions, and chemical reactions under conditions similar to those during growth or device operation. This field has been developed and integrated over many years into materials science [233]. In the last decade, in-situ TEM techniques received a lot of attention due to the promise of combining high spatial resolution with in-situ techniques so researchers can observe the behaviour of semiconductor materials and devices with time-resolution at the nanoscale. In-situ TEM techniques allow for the precise characterization of semiconductor materials and devices under various environmental conditions, such as temperature, pressure and electrical bias.

5.1 In-situ environment

In-situ measurements include the use of environmental transmission electron microscopy (ETEM) which allows the observation of materials and processes in a controlled gaseous environment, or by employing specific in-situ holders that directly provide the required environmental conditions for the sample [234],[235]. The principle behind these in-situ holders is to create a controllable environment around the sample using specifically designed micro electro-mechanical systems (MEMS) while maintaining a good vacuum throughout the TEM column. These holders are designed to accommodate samples under specific environmental conditions or apply stimuli, such as heating, cooling, applying electrical bias, applying magnetic fields, mechanical stress, or exposure to gases (Figure 13) [236]-[238]. For example, as shown in Figure 13, this is a heating holder from Protochips that provides a platform for precise temperature control, ultra-low drift, temperatures up to 1,200 ˚C and ramp rates up to 1,000 ˚C per millisecond.

Accepted Manuscript

1
2
3
4
5
6
7
8
9
10
11
12
13
14
15
16
17
18
19
20
21
22
23
24
25
26
27
28
29
30
31
32
33
34
35
36
37
38
39
40
41
42
43
44
45
46
47
48
49
50
51
52
53
54
55
56
57
58
59
60

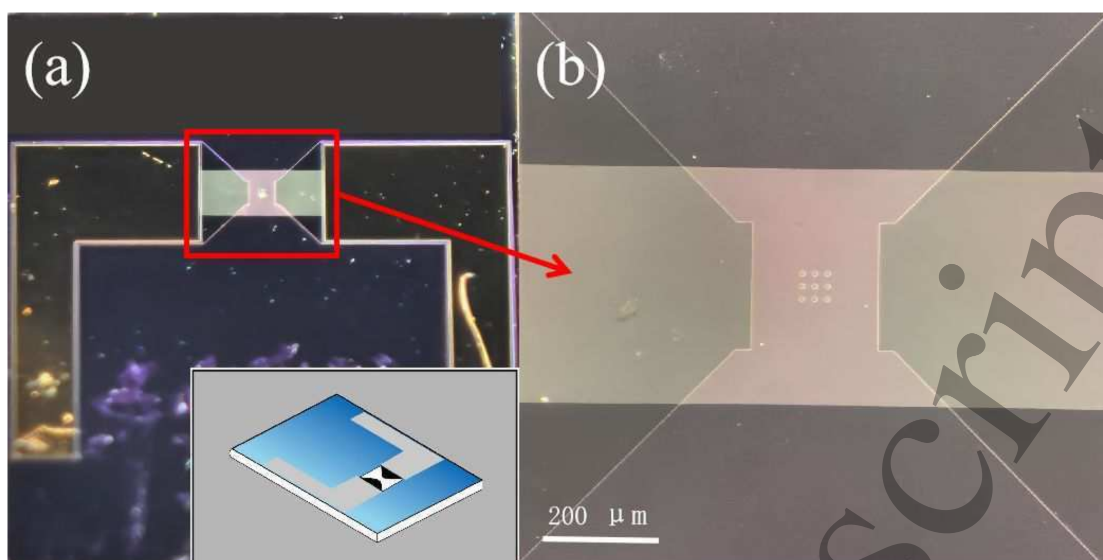

Fig. 13. (a) In-situ heating holders (the illustration is a schematic diagram, the gray part represents the electrodes); (b) Micrometer-scale nanoporous film (Fig.(a) enlarged portion of the red box).

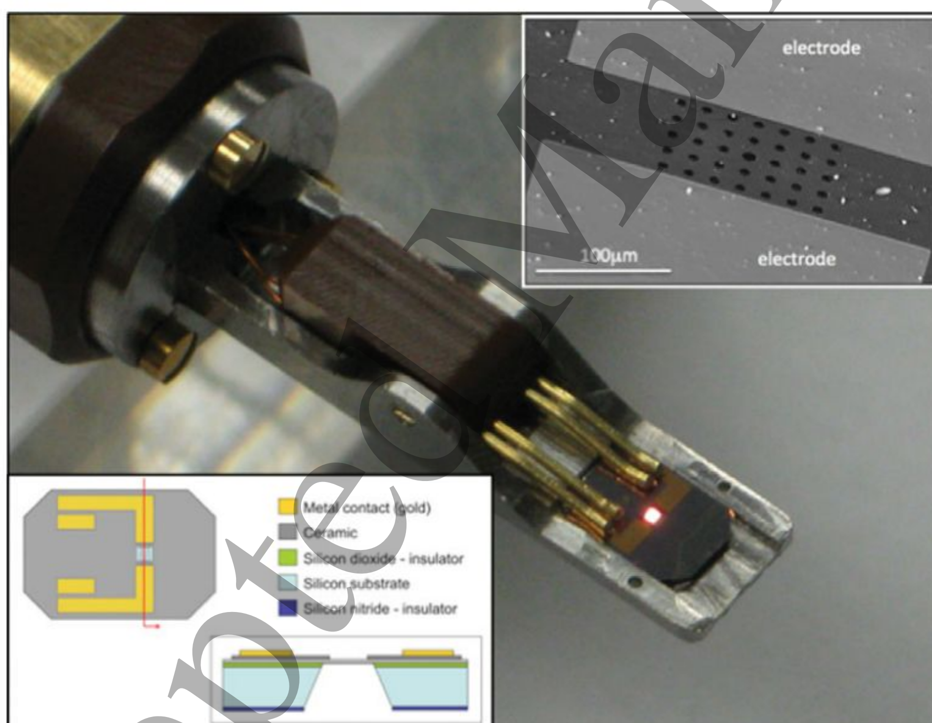

Fig.14. Standard Aduro^{TM} heater device installed in a single-tilt specimen holder and heated to 1000℃ in air. The cross-section schematic inset illustrates the components of the micro electro-mechanical system (MEMS) device, and the top view shows the configuration of Au electrodes on the upper surface of the device that provide contacts for current to be passed through the heater membrane. The SEM image inset shows a typical pattern of holes in the heater

Accepted Manuscript

1 2 3 4 5 6 7 8 9 10 11 12 13 14 15 16 17 18 19 20 21 22 23 24 25 26 27 28 29 30 31 32 33 34 35 36 37 38 39 40 41 42 43 44 45 46 47 48 49 50 51 52 53 54 55 56 57 58 59 60

membrane, which support, for example, a thin carbon film that in turn supports deposited material [239].

Another approach is to create a separate space where the sample can be pressurized and heated from within. The electron beam can then enter this independent sample chamber through a specially designed silicon nitride window. This silicon nitride can be very thin (down to 20nm) and then may have little effect on the entry of high-energy electron beams, as shown in Figure 14 [239].

5.2 In-situ temporal and spatial resolution

In-situ electron microscopy allows for continuous observations. Zewail et al. [240] were the first to synchronize a femtosecond laser source with a laser beam on the sample to achieve high temporal resolution in electron diffraction. This method keeps only one electron in the column at any given time to reduce space charge effects, but the electron beam must be continuously emitted and the electron beam should not damage the sample or cause damage that has not healed before the next electron-sample contact. The intensity of this approach limits its widespread use. Another method, pioneered by Bostanjoglo et al., creates an image in a single shot by generating a longer pulse with sufficient electrons [241]. The single-pulse process does not need to be reversible because all information is obtained from a single electron pulse. The limitation of this method is that space charge effects in the beam can cause resolution degradation, and even with optimized microscope sources, columns, and detectors, high currents can limit the overall temporal and spatial resolution of the instrument.

5.3 In-situ technology application

Currently, in-situ techniques play an important role in understanding the electronic states of microstructures and the chemical evolution in the growth of nanoscale devices made of multi-component semiconductors [242]. By observing and analyzing the changes in materials in real-time, information about the electronic states of microstructures can be obtained, including band structures, binding states, charge carrier behaviour, etc., which can provide a deeper understanding of the properties of materials [243],[244]. Current specimen holders have advanced

Accepted Manuscript

1
2
3
4
5
6
7
8
9
10
11
12
13
14
15
16
17
18
19
20
21
22
23
24
25
26
27
28
29
30
31
32
33
34
35
36
37
38
39
40
41
42
43
44
45
46
47
48
49
50
51
52
53
54
55
56
57
58
59
60

to the point where compression, tension, or bending experiments can be conducted at temperatures as low as –140°C or as high as ±400°C to quantify the levels of strength and ductility. These holders also possess high stability, enabling high-resolution stress measurements with a force resolution better than 1 μN and displacement resolution of 1 nm [245], which is extremely suitable to investigate semiconductor nanowires.

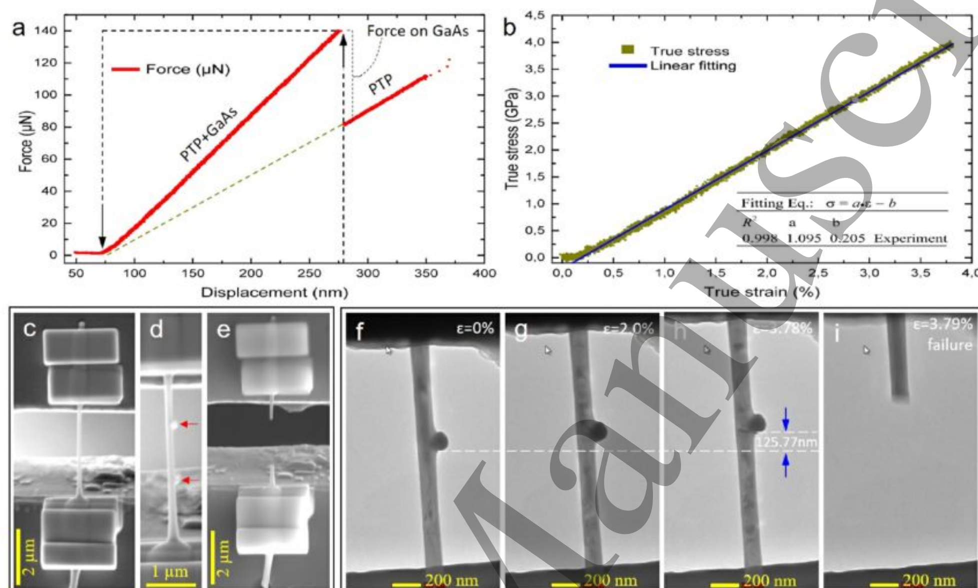

Fig. 15. Uniaxial tensile deformation of a single GaAs nanowire along the [111] growth orientation. (a) Experimental method showing calculation of the force loaded on the single GaAs nanowire. (b) Representative stress-strain curve of the GaAs nanowire under uniaxial tensile straining. (c)–(e) SEM images of the GaAs nanowire before and after fracture, with two FIB-deposited Pt markers (red arrows in (d)) as reference for strain measurement. (f)–(i) TEM images of the GaAs nanowire at different applied strains of 0%, 2.0%, 3.78% and 3.79%/failure [246].

Nanowire devices have been widely applied in fields such as optoelectronics, sensors, generators, and spectroscopy. Understanding the mechanical properties of nanowires has become increasingly necessary. In their study of GaAs nanowires with a diameter of 120 nm grown using MOVPE, Liu et al. [246] investigated the mechanical properties and fracture mechanisms of single-phase GaAs nanowires through in-situ uniaxial tensile deformation experiments and molecular dynamics simulations. As shown in Figure 15, the research results indicate that under tensile stress, GaAs

Accepted Manuscript

nanowires exhibit overall elastic deformation until they suddenly experience brittle fracture at a strain of 3.79%.

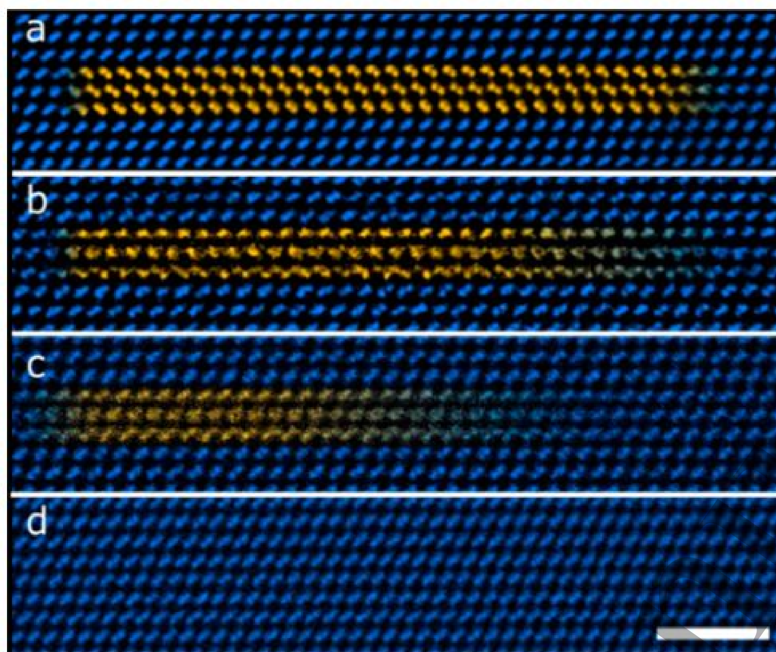

Fig.16. ADF-STEM images of 3 monolayer (ML) microtwin defects in a type 1 configuration (right) and type 2 configuration (left), during exposure to increasing temperatures. (a) Before heating and after (b) heating at 680°C for 30 minutes, (c) heating at 680°C continued for 30 minutes, and (d) heating up to 700°C for 30 minutes, at which point the twin has been completely removed from the nanowire. Scale bar is 2 nm [247]. Colour visualizes the orientation of the dumb-bells.

Real-time observation of defect changes during semiconductor annealing helps people understand the structural properties of materials. The consumption of liquid droplets in self-catalyzed III-V semiconductor nanowire growth can result in material with a high-density of line defects. Gott et al. [247] used in-situ aberration-corrected scanning transmission electron microscopy to analyze the stability of GaAsP NWs under short annealing periods, as shown in Figure 16. The atomic arrangement marked by yellow color demonstrates the twin defects in GaAsP [247]. By observing the movement of individual microtwin defects, it was found that their motion depended on their size, position, and surrounding environment, and the upper limit of activation energy was measured at around 2 eV. After annealing at 640°C following growth at the same temperature,

Accepted Manuscript

most defects (>70%) were removed in GaAsP NWs, demonstrating that in-situ annealing during the growth at lower growth temperatures significantly improves material quality.

For more complex crystallization processes, in-situ technology can also help, displaying the crystallization processes. Gas-phase grown Si or Ge thin films are usually amorphous, and their crystallization requires external stimuli to undergo the transition from metastable to equilibrium states, by thermal annealing, stress, electron or laser beam irradiation, which can all serve as external stimuli for triggering the above transition [248]-[252]. Annealing of amorphous Ge films induces their crystallization within the temperature range of 400-590 ℃ [253]-[255]. This effect is often referred to as "metal-induced" or "metal-mediated" crystallization (MIC), and the basic mechanism of the MIC reaction is still controversial. Kryshtal et al. [256] used in-situ aberration corrected TEM/STEM combined with EDXS and EELS to study the initial stages of the MIC process to understand and determine the MIC mechanism.

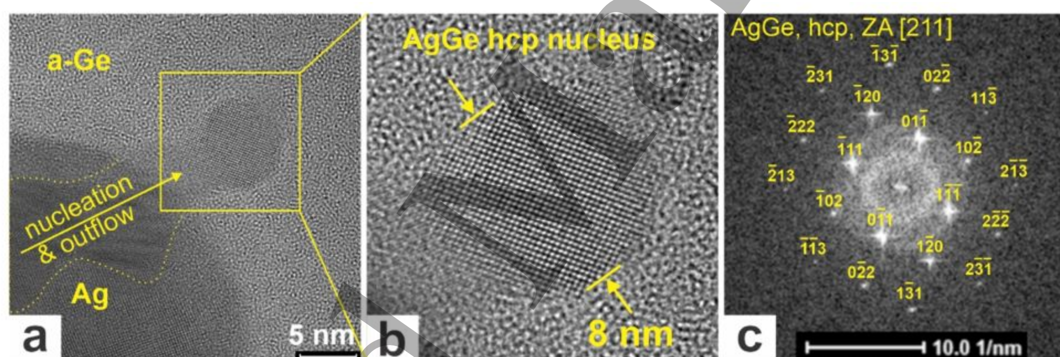

Fig. 17. Phase contrast TEM images (a, b) of AgGe nucleus at 450℃ and FFT of (b) indexed as AgGe hcp phase (c). Dotted line in (a) outlines the area of MIC reaction at the Ag-Ge interface [256].

Research has found that atomic nuclei formed at an Ag-Ge interface can migrate freely into the free region of the Ag-Ge film. In the experiment, it was observed that an atomic nucleus located at the edge of Ag-NP exhibited a spherical shape of approximately 8 nm (Figure 17(b)). During the observation process, it was noted that the atomic nucleus was unstable. The research findings ultimately indicated that the atomic nucleus remained stationary for several seconds and then advanced in a jumping manner to the adjacent a-Ge region, leaving behind crystalline Ge. This process was repeated several times, resulting in the crystallization of a-Ge around the parent

Accepted Manuscript

1
2
3
4
5
6
7
8
9
10
11
12
13
14
15
16
17
18
19
20
21
22
23
24
25
26
27
28
29
30
31
32
33
34
35
36
37
38
39
40
41
42
43
44
45
46
47
48
49
50
51
52
53
54
55
56
57
58
59
60

Ag-NP, as shown in Figure 18 [256].

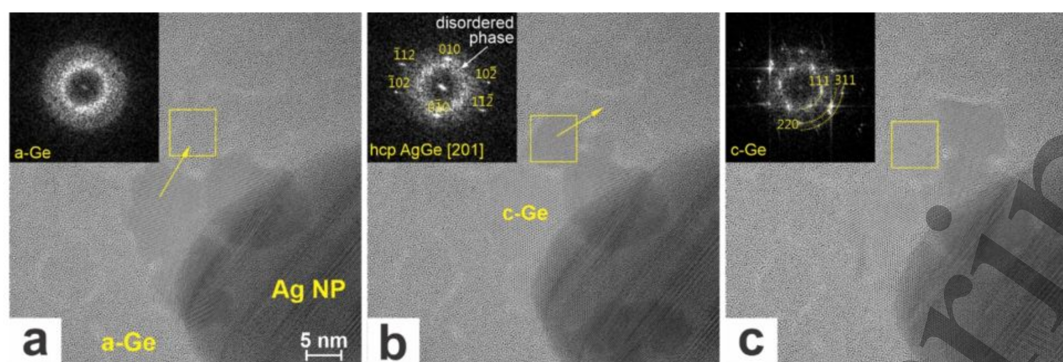

Fig. 18. Time series of TEM images of the same area of Ag/Ge film at 450°C showing the propagation of a nucleus and crystallization of a-Ge film. FFT spectrum in the inset corresponds to the rectangular region. Arrows in TEM images indicate the direction of the nucleus advancement. Dotted arcs in the inset in (c) correspond to crystalline Ge [256].

Observation and analysis indicate that the hcp-AgGe phase is formed through crystallization of a non-equilibrium liquid-phase eutectic alloy, rather than sacrificing the excess energy of the a-Ge film. This supports the liquid-phase mechanism of the MIC reaction.

In-situ techniques allow for real-time monitoring and analysis of the evolution process of chemical compositions. By observing and analyzing the changes in images, key information such as atomic composition distribution, interatomic interactions, and interface properties can be explored. This helps understand the dynamics and influencing factors of material growth, providing guidance for optimizing device performance and fabrication processes [257]-[259].

5.4 Challenges of the in-situ TEM technologies for semiconductor research

In-situ TEM techniques are important for observing the dynamic behaviour of the semiconductor materials or devices in real-time. In-situ techniques allow for the observation of structural evolution and phase transformation processes, as well as dynamic behaviour such as crystal growth and dislocation motion, by applying or varying in TEM external conditions such as temperature, electric fields, and mechanical stress [260],[261]. They provide valuable information for interface engineering and material design by observing and analyzing processes such as diffusion and reaction at material interfaces.

Despite significant progress, in-situ electron microscopy still faces substantial challenges. The

Accepted Manuscript

1 2 3 4 5 6 7 8 9 10 11 12 13 14 15 16 17 18 19 20 21 22 23 24 25 26 27 28 29 30 31 32 33 34 35 36 37 38 39 40 41 42 43 44 45 46 47 48 49 50 51 52 53 54 55 56 57 58 59 60

first is electron beam damage, the destructive interaction between high-energy electron beams and sample materials that relates characterization results obtained through TEM to real-world environments. In-situ electron microscopy needs to simulate real-world environments to observe their effects on materials, but some materials are more susceptible to electron beam damage than others. To address this issue, a standardized rule for evaluating damage requires cooperation from scientists in various fields. Determining electron beam damage is complex and involves many factors, such as material properties, sample thickness, electron energy, and electron irradiation time.

The second is that the idea of in-situ or in-operando measurements is to measure properties under conditions that resemble real growth conditions or device operation conditions as closely as possible, however, the free surfaces of electron transparent specimens will always be there and can influence and may even falsify measurements because

a) oxide surfaces behave differently to freshly cleaved crystal surfaces [262],
b) FIB preparation, as often needed to create electron transparent specimens from device-type material, always leads to some degree of ion implantation and surface damage [69],
c) electron irradiation damage can bias or completely change the results, in particular if properties are measured that are related to the critical behaviour of minority charge carriers (e.g. electrical conductivity) or a small number density of minority atoms (e.g. brittleness of grain boundary) [263]. A thin lamella specimen under electron flux will likely never reach thermal equilibrium as a bulk specimen does.

The third challenge is measuring sample temperature accurately. Due to environmental interference, such as by pressure and humidity in experiments, existing temperature-pressure gradient formulas must be adopted [264]. For example, using electron energy-loss spectroscopy to measure local temperature and gas density variation with temperature in a window bracket filled with 1.25 Pa H_2 gives consistent results. Still, this method has limitations and significant measurement errors in more complex gas environments [265].

The fourth challenge is high spatial and temporal resolution with a sufficiently large field of view. Available image acquisition systems allow us to obtain either high temporal or high spatial resolution images. The direct electron detection cameras based on complementary

Accepted Manuscript

1 2 3 4 5 6 7 8 9 10 11 12 13 14 15 16 17 18 19 20 21 22 23 24 25 26 27 28 29 30 31 32 33 34 35 36 37 38 39 40 41 42 43 44 45 46 47 48 49 50 51 52 53 54 55 56 57 58 59 60

metal-oxide-semiconductor technology can improve temporal resolution without affecting spatial resolution, but their high cost prevents widespread usage.

Finally, after addressing the above issues, multiple detection methods need to be combined, such as simultaneously recording images, DPs and EDXS/EELS maps, to compare and discover valuable information. However, existing instruments do not routinely output signals from different detectors simultaneously, especially if software and/or detector hardware are from different manufacturers.

6. **Conclusion and Outlook**

Transmission electron microscopy is a technique that utilizes an electron beam to transmit through a thinned sample, and the generated signals can be detected to obtain information about the material. The method has high spatial resolution and some modes reach the atomic scale, allowing for the characterization of not only crystal structures/chemical compositions but also strain, defects and bandgap in semiconductor materials. Combining various TEM characterization methods at different scales helps to understand the physics behind them, providing valuable information for device improvement.

In-situ techniques make real-time observation and analysis possible. The development of in-situ techniques will provide insight into growth mechanisms, phase transitions, and the evolution of structure-property relationships. However, current research is often limited to conducting one test at a time, and it cannot simultaneously acquire multiple types of information. Moreover, achieving real-time monitoring remains challenging.

AUTHOR DECLARATIONS

Conflict of Interest

The authors have no conflicts to disclose.

ACKNOWLEDGMENTS

This work was supported by the Department of Science and Technology of Sichuan Province (grant number: 2023YFH0054), the Technology and Innovation Commission of the Shenzhen Municipality (grant number: JCYJ20190809142019365), Zhejiang Province "Vanguard Leading

Accepted Manuscript

Geese + X" Project (grant number:2024SSYS0045) and the Fundamental Research Funds for the Central Universities of Southwest Minzu University (grant number: ZYN2024127).

References

[1] Asahi, H., and Horikoshi, Y., eds. Molecular Beam Epitaxy: Materials and applications for electronics and optoelectronics[M]. John Wiley & Sons, 2019.

[2] Bosi M, Attolini G. Germanium: Epitaxy and its applications[J]. Progress in Crystal Growth and Characterization of Materials, 2010, 56(3-4): 146-174.

[3] Bosi M, Pelosi C. The potential of III-V semiconductors as terrestrial photovoltaic devices[J]. Progress in Photovoltaics: Research and Applications, 2007, 15(1): 51-68.

[4] Awschalom D D, Flatté M E. Challenges for semiconductor spintronics[J]. Nature Physics, 2007, 3(3): 153-159.

[5] Park Y D, Hanbicki A T, Erwin S C, et al. A group-IV ferromagnetic semiconductor: Mn_xGe_{1-x}[J]. Science, 2002, 295(5555): 651-654.

[6] Markov I, Stoyanov S. Mechanisms of epitaxial growth[J]. Contemporary physics, 1987, 28(3): 267-320.

[7] Lewis B. Physical processes in epitaxial growth[J]. Thin Solid Films, 1971, 7(3-4): 179-217.

[8] Cho A Y, Arthur J R. Molecular beam epitaxy[J]. Progress in solid state chemistry, 1975, 10: 157-191.

[9] Cho A Y. Recent developments in molecular beam epitaxy (MBE)[J]. Journal of Vacuum Science and Technology, 1979, 16(2): 275-284.

[10] Kuech T F. Metal-organic vapor phase epitaxy of compound semiconductors[J]. Materials Science Reports, 1987, 2(1): 1-49.

[11] Gibart P. Metal organic vapour phase epitaxy of GaN and lateral overgrowth[J]. Reports on Progress in Physics, 2004, 67(5): 667.

[12] Koukitu A, Kumagai Y. Thermodynamic analysis of group III nitrides grown by metal-organic vapour-phase epitaxy (MOVPE), hydride (or halide) vapour-phase epitaxy (HVPE) and molecular beam epitaxy (MBE)[J]. Journal of Physics: Condensed Matter, 2001, 13(32): 6907.

[13] Ko T S, Wang T C, Gao R C, et al. Study on optimal growth conditions of a-plane GaN

Accepted Manuscript

grown on r-plane sapphire by metal-organic chemical vapor deposition[J]. Journal of Crystal Growth, 2007, 300(2): 308-313.

[14] Lei T, Moustakas T D, Graham R J, et al. Epitaxial growth and characterization of zinc-blende gallium nitride on (001) silicon[J]. Journal of Applied Physics, 1992, 71(10): 4933-4943.

[15] Pashley D W. Epitaxy growth mechanisms[J]. Materials Science and Technology, 1999, 15(1): 2-8.

[16] Walther T, Cullis A G, Norris D J, et al. Nature of the Stranski-Krastanow transition during epitaxy of InGaAs on GaAs[J]. Physical Review Letters, 2001, 86(11): 2381.

[17] Lozovoy K A, Korotaev A G, Kokhanenko A P, et al. Kinetics of epitaxial formation of nanostructures by Frank–van der Merwe, Volmer–Weber and Stranski–Krastanow growth modes[J]. Surface and Coatings Technology, 2020, 384: 125289.

[18] Bagmut A G. Layer, island and dendrite crystallizations of amorphous films as analogs of Frank-van der Merwe, Volmer-Weber and Stranski-Krastanov growth modes[J]. 2019.

[19] Barnett S J, Keir A M, Cullis A G, et al. In situ X-ray topography studies during the molecular beam epitaxy growth of InGaAs on (001) GaAs: effects of substrate dislocation distribution on strain relaxation[J]. Journal of Physics D: Applied Physics, 1995, 28(4A): A17.

[20] Tessarek C, Figge S, Aschenbrenner T, et al. Strong phase separation of strained $In_xGa_{1-x}N$ layers due to spinodal and binodal decomposition: Formation of stable quantum dots[J]. Physical Review B, 2011, 83(11): 115316.

[21] Tillmann K, Thust A, Lentzen M, et al. Determination of segregation, elastic strain and thin-foil relaxation in In_xGa_{1-x} As islands on GaAs (001) by high resolution transmission electron microscopy[J]. Philosophical magazine letters, 1996, 74(5): 309-315.

[22] Walther, Thomas, et al. "Study of phase separation in an InGaN alloy by electron energy loss spectroscopy in an aberration corrected monochromated scanning transmission electron microscope." Journal of Materials Research 32.5 (2017): 983-995.

[23] Jinschek J R, Erni R, Gardner N F, et al. Local indium segregation and bang gap variations in high efficiency green light emitting InGaN/GaN diodes[J]. Solid State Communications, 2006, 137(4): 230-234.

[24] Tourbot G, Bougerol C, Grenier A, et al. Structural and optical properties of InGaN/GaN

Accepted Manuscript

1 2 3 4 5 6 7 8 9 10 11 12 13 14 15 16 17 18 19 20 21 22 23 24 25 26 27 28 29 30 31 32 33 34 35 36 37 38 39 40 41 42 43 44 45 46 47 48 49 50 51 52 53 54 55 56 57 58 59 60

nanowire heterostructures grown by PA-MBE[J]. Nanotechnology, 2011, 22(7): 075601.

[25] Yi, Gyu-Chul, ed. Semiconductor nanostructures for optoelectronic devices: processing, characterization and applications[M]. Springer Science & Business Media, 2012.

[26] Feng, Z. C.ed .III-Nitride semiconductor materials[M]. World Scientific, 2006.

[27] Pearton S J, Shul R J, Wolfgang E, et al. Power semiconductor materials and devices[R]. Materials Research Society, Warrendale, PA (US), 1997.

[28] Hong, M. , et al. In-situ process for AlGaAs compound semiconductor: Materials science and device fabrication[J]. Journal of Electronic Materials 23.7(1994):625-634.

[29] Kajiwara, K. , and H. Kawai . Analysis of AlGaAs/GaAs superlattices by means of sputter-assisted AES, SEM and TEM[J]. Surface & Interface Analysis 15.7(1990):433–439.

[30] Rai R S, Subramanian S. Role of transmission electron microscopy in the semiconductor industry for process development and failure analysis[J]. Progress in crystal growth and characterization of materials, 2009, 55(3-4): 63-97.

[31] Thomas G, Goringe M J. Transmission electron microscopy of materials[J]. 1979.

[32] Spence J C H. High-resolution electron microscopy[M]. OUP Oxford, 2013.

[33] Pennycook S J, Boatner L A. Chemically sensitive structure-imaging with a scanning transmission electron microscope[J]. Nature, 1988, 336(6199): 565-567.

[34] Browning N D, Chisholm M F, Pennycook S J. Atomic-resolution chemical analysis using a scanning transmission electron microscope[J]. Nature, 1993, 366(6451): 143-146.

[35] Xu, Zhi, et al. Real-time in situ HRTEM-resolved resistance switching of Ag_2S nanoscale ionic conductor[J]. ACS nano 4.5 (2010): 2515-2522.

[36] Abd Mutalib, M., et al. Scanning electron microscopy (SEM) and energy-dispersive X-ray (EDX) spectroscopy[J]. Membrane characterization. Elsevier, 2017. 161-179.

[37] Gürbulak, Bekir, et al. Structural characterizations and optical properties of InSe and InSe: Ag semiconductors grown by Bridgman/Stockbarger technique[J]. Physica E: Low-dimensional Systems and Nanostructures 64 (2014): 106-111.

[38] Laskin, Alexander, and James P. Cowin. Automated single-particle SEM/EDX analysis of submicrometer particles down to 0.1 μm[J].Analytical Chemistry 73.5 (2001): 1023-1029.

[39] De Graef M. Introduction to conventional transmission electron microscopy[M]. Cambridge university press, 2003.

Accepted Manuscript

1
2
3
4
5
6
7
8
9
10
11
12
13
14
15
16
17
18
19
20
21
22
23
24
25
26
27
28
29
30
31
32
33
34
35
36
37
38
39
40
41
42
43
44
45
46
47
48
49
50
51
52
53
54
55
56
57
58
59
60

[40] Kohl H, Reimer L. Transmission Electron Microscopy[J]. Springer Series in Optical Sciences, 2008, 36.

[41] Pennycook S J, Boatner L A. Chemically sensitive structure-imaging with a scanning transmission electron microscope[J]. Nature, 1988, 336(6199): 565-567.

[42] Browning N D, Chisholm M F, Pennycook S J. Atomic-resolution chemical analysis using a scanning transmission electron microscope[J]. Nature, 1993, 366(6451): 143-146.

[43] Inkson B J. Scanning electron microscopy (SEM) and transmission electron microscopy (TEM) for materials characterization[M]//Materials characterization using nondestructive evaluation (NDE) methods. Woodhead publishing, 2016: 17-43.

[44] Kaiser U, Biskupek J, Meyer J C, et al. Transmission electron microscopy at 20 kV for imaging and spectroscopy[J]. Ultramicroscopy, 2011, 111(8): 1239-1246.

[45] Utsunomiya S, Ewing R C. Application of high-angle annular dark field scanning transmission electron microscopy, scanning transmission electron microscopy-energy dispersive X-ray spectrometry, and energy-filtered transmission electron microscopy to the characterization of nanoparticles in the environment[J]. Environmental science & technology, 2003, 37(4): 786-791.

[46] Batson P E, Dellby N, Krivanek O L. Sub-ångstrom resolution using aberration corrected electron optics[J]. Nature, 2002, 418(6898): 617-620.

[47] Haider M, Uhlemann S, Schwan E, et al. Electron microscopy image enhanced[J]. Nature, 1998, 392(6678): 768-769.

[48] Lazić, Ivan, Eric GT Bosch, and Sorin Lazar. Phase contrast STEM for thin samples: Integrated differential phase contrast[J]. Ultramicroscopy 160 (2016): 265-280.

[49] N. H. Dekkers, H. de Lang, Differential phase contrast in a STEM. Optik 41, 452–456 (1974).

[50] Shibata, Naoya, et al. Differential phase-contrast microscopy at atomic resolution[J]. Nature Physics 8.8 (2012): 611-615.

[51] Abd Mutalib, M., et al. Scanning electron microscopy (SEM) and energy-dispersive X-ray (EDX) spectroscopy[J]. Membrane characterization. Elsevier, 2017. 161-179.

[52] Amari H, Zhang H Y, Geelhaar L, et al. Nanoscale EELS analysis of elemental distribution and band-gap properties in AlGaN epitaxial layers[J]. Journal of Physics: Conference Series. IOP

Accepted Manuscript

Publishing, 2011, 326(1): 012039.

[53] Sato K, Takenaka K, Makino A, et al. Structural heterogeneity of the melt-spun (Fe, Co)-Si-BP-Cu alloy with excellent soft magnetic properties[J]. Physics Procedia, 2015, 75: 1376-1380.

[54] Tsuda K, Mitsuishi H, Terauchi M, et al. Strain analysis of arsenic-doped silicon using CBED rocking curves of low-order reflections[J]. Journal of electron microscopy, 2007, 56(2): 57-61.

[55] Zuo J M, Spence J C H. Advanced transmission electron microscopy[M]. New York: Springer Science Business Media, 2017.

[56] He B, Zhang Y, Liu X, et al. In-situ transmission electron microscope techniques for heterogeneous catalysis[J]. ChemCatChem, 2020, 12(7): 1853-1872.

[57] Deng Y, Zhang R, Pekin T C, et al. Functional materials under stress: In situ TEM observations of structural evolution[J]. Advanced materials, 2020, 32(27): 1906105.

[58] Zschech E, Engelmann H J, Meyer M A, et al. Effect of interface strength on electromigration-induced inlaid copper interconnect degradation: Experiment and simulation[J]. International Journal of Materials Research, 2022, 96(9): 966-971.

[59] Rao D V S, Muraleedharan K, Humphreys C J. TEM specimen preparation techniques[J]. Microscopy: science, technology, applications and education, 2010, 2: 1232.

[60] Thompson-Russell K C, Edington J W, Thompson-Russell K C, et al. Electron microscope specimen preparation techniques in materials science[M]. Macmillan Education UK, 1977.

[61] Barber D J. Thin foils of non-metals made for electron microscopy by sputter-etching[J]. Journal of Materials Science, 1970, 5: 1-8.

[62] Barna Á. Topographic kinetics and practice of low angle ion beam thinning[J]. MRS Online Proceedings Library (OPL), 1991, 254: 3.

[63] Wang X. Characterization of InGaN thin films and nanowires by analytical transmission electron microscopy[D]. University of Sheffield, 2018.

[64] Giannuzzi, Lucille A., ed. Introduction to focused ion beams: instrumentation, theory, techniques and practice[M]. Springer Science & Business Media, 2004.

[65] Harriott L R. The technology of finely focused ion beams[J]. Nuclear Instruments and Methods in Physics Research Section B: Beam Interactions with Materials and Atoms, 1991, 55(1-4): 802-810.

Accepted Manuscript

1
2
3
4
5
6
7
8
9
10
11
12
13
14
15
16
17
18
19
20
21
22
23
24
25
26
27
28
29
30
31
32
33
34
35
36
37
38
39
40
41
42
43
44
45
46
47
48
49
50
51
52
53
54
55
56
57
58
59
60

[66] Yao, Nan, ed. Focused ion beam systems: basics and applications[M]. Cambridge University Press, 2007.

[67] Harriott L R. The technology of finely focused ion beams[J]. Nuclear Instruments and Methods in Physics Research Section B: Beam Interactions with Materials and Atoms, 1991, 55(1-4): 802-810.

[68] Wirth R. Focused Ion Beam (FIB) combined with SEM and TEM: Advanced analytical tools for studies of chemical composition, microstructure and crystal structure in geomaterials on a nanometre scale[J]. Chemical Geology, 2009, 261(3-4): 217-229.

[69] Ma Z, Zhang X, Liu P, et al. Clustering in gallium ion beam sputtered compound materials driven by bond strength and interstitial/vacancy reaction[J]. Applied Physics Letters, 2023, 123(10).

[70] Li J, Malis T, Dionne S. Recent advances in FIB–TEM specimen preparation techniques[J]. Materials characterization, 2006, 57(1): 64-70.

[71] Mayer J, Giannuzzi L A, Kamino T, et al. TEM sample preparation and FIB-induced damage[J]. MRS bulletin, 2007, 32(5): 400-407.

[72] Hÿtch M J, Snoeck E, Kilaas R. Quantitative measurement of displacement and strain fields from HREM micrographs[J]. Ultramicroscopy, 1998, 74(3): 131-146.

[73] Ji G, Morniroli J P, Auchterlonie G J, et al. An efficient approach to characterize pseudo-merohedral twins by precession electron diffraction: Application to the $LaGaO_3$ perovskite[J]. Ultramicroscopy, 2009, 109(10): 1282-1294.

[74] Béché A, Rouvière J L, Barnes J P, et al. Strain measurement at the nanoscale: Comparison between convergent beam electron diffraction, nano-beam electron diffraction, high resolution imaging and dark field electron holography[J]. Ultramicroscopy, 2013, 131: 10-23.

[75] Gabor D. Microscopy by reconstructed wave-fronts[J]. Proceedings of the Royal Society of London. Series A. Mathematical and Physical Sciences, 1949, 197(1051): 454-487.

[76] Smith D J. Atomic-resolution structure imaging of defects and interfaces in compound semiconductors[J]. Progress in Crystal Growth and Characterization of Materials, 2020, 66(4): 100498.

[77] T. Walther, C.J. Humphreys: A quantitative study of compositional profiles of chemical vapour-deposited strained silicon-germanium / silicon layers by transmission electron

Accepted Manuscript

1
2
3
4
5
6
7
8
9
10
11
12
13
14
15
16
17
18
19
20
21
22
23
24
25
26
27
28
29
30
31
32
33
34
35
36
37
38
39
40
41
42
43
44
45
46
47
48
49
50
51
52
53
54
55
56
57
58
59
60

microscopy[J]. J. Crystal Growth 197:1-2 (1999) 113-128.

[78] T. Walther, C.J. Humphreys: The limitations of pattern recognition and displacement measurement techniques for evaluating HREM images of strained semiconductor interfaces[J]. Proc. EMAG95, Birmingham. Inst. Phys. Conf. Ser. 147 (1995) 103-106.

[79] Sarigiannidou E, Monroy E, Daudin B, et al. Strain distribution in GaN/AlN quantum-dot superlattices[J]. Applied Physics Letters, 2005, 87(20).

[80] Wen C Y, Reuter M C, Su D, et al. Strain and stability of ultrathin Ge layers in Si/Ge/Si axial heterojunction nanowires[J]. Nano letters, 2015, 15(3): 1654-1659.

[81] Wang Y, Liu X P, Qin G W. The strain models of complex misfit dislocations at α-Fe_2O_3/α-Al_2O_3 interface[J]. Scripta Materialia, 2015, 109: 11-14.

[82] Rösner H, Koch C T, Wilde G. Strain mapping along Al–Pb interfaces[J]. Acta materialia, 2010, 58(1): 162-172.

[83] Qiu Y, Cristiano F, Huet K, et al. Extended defects formation in nanosecond laser-annealed ion implanted silicon[J]. Nano Letters, 2014, 14(4): 1769-1775.

[84] Kang S, Wang D, Kübel C, et al. Importance of TEM sample thickness for measuring strain fields[J]. Ultramicroscopy, 2024, 255: 113844.

[85] Benzo P. Stress transfer in ultimate transistors through SiN deposits: study by electron holography and finite element modelling[D]. Toulouse 3, 2013.

[86] Van Aert S, Verbeeck J, Erni R, et al. Quantitative atomic resolution mapping using high-angle annular dark field scanning transmission electron microscopy[J]. Ultramicroscopy, 2009, 109(10): 1236-1244.

[87] Leary R, Saghi Z, Armbrüster M, et al. Quantitative high-angle annular dark-field scanning transmission electron microscope (HAADF-STEM) tomography and high-resolution electron microscopy of unsupported intermetallic GaPd2 catalysts[J]. The Journal of Physical Chemistry C, 2012, 116(24): 13343-13352.

[88] Utsunomiya S, Ewing R C. Application of high-angle annular dark field scanning transmission electron microscopy, scanning transmission electron microscopy-energy dispersive X-ray spectrometry, and energy-filtered transmission electron microscopy to the characterization of nanoparticles in the environment[J]. Environmental science & technology, 2003, 37(4): 786-791.

Accepted Manuscript

[89] Perovic D D, Rossouw C J, Howie A. Imaging elastic strains in high-angle annular dark field scanning transmission electron microscopy[J]. Ultramicroscopy, 1993, 52(3-4): 353-359.

[90] Park B, Lee J K, Koch C T, et al. High-resolution mapping of strain partitioning and relaxation in InGaN/GaN nanowire heterostructures[J]. Advanced Science, 2022, 9(22): 2200323.

[91] Debelle, Aurelien, and Alain Declemy. XRD investigation of the strain/stress state of ion-irradiated crystals. Nuclear Instruments and Methods in Physics Research Section B: Beam Interactions with Materials and Atoms 268.9 (2010): 1460-1465.

[92] Harutyunyan, V. S., et al.High-resolution x-ray diffraction strain-stress analysis of GaN/sapphire heterostructures. Journal of Physics D: Applied Physics 34.10A (2001): A35.

[93] Kidd, P. XRD of gallium nitride and related compounds: strain, composition and layer thickness. Panalytical: Almelo, Netherlands (2009): 119.

[94] Cooper D, Denneulin T, Bernier N, et al. Strain mapping of semiconductor specimens with nm-scale resolution in a transmission electron microscope[J]. Micron, 2016, 80: 145-165.

[95] Mills S H, Zeltmann S E, Ercius P, et al. Nanoscale mapping of point defect concentrations with 4D-STEM[J]. Acta Materialia, 2023, 246: 118721.

[96] Barnard J S, Johnstone D N, Midgley P A. High-resolution scanning precession electron diffraction: Alignment and spatial resolution[J]. Ultramicroscopy, 2017, 174: 79-88.

[97] Flannigan D J, Zewail A H. 4D electron microscopy: Principles and applications[J]. Accounts of chemical research, 2012, 45(10): 1828-1839.

[98] Humphreys C J. The significance of Bragg's law in electron diffraction and microscopy, and Bragg's second law[J]. Acta Crystallographica Section A: Foundations of Crystallography, 2013, 69(1): 45-50.

[99] Zuo J M, Gao M, Tao J, et al. Coherent nano-area electron diffraction[J]. Microscopy research and technique, 2004, 64(5-6): 347-355.

[100] Béché A, Rouvière J L, Clément L, et al. Improved precision in strain measurement using nanobeam electron diffraction[J]. Applied Physics Letters, 2009, 95(12).

[101] Usuda K, Mizuno T, Tezuka T, et al. Strain relaxation of strained-Si layers on SiGe-on-insulator (SGOI) structures after mesa isolation[J]. Applied surface science, 2004, 224(1-4): 113-116.

[102] Armigliato A, Frabboni S, Gazzadi G C. Electron diffraction with ten nanometer beam size

Accepted Manuscript

1 2 3 4 5 6 7 8 9 10 11 12 13 14 15 16 17 18 19 20 21 22 23 24 25 26 27 28 29 30 31 32 33 34 35 36 37 38 39 40 41 42 43 44 45 46 47 48 49 50 51 52 53 54 55 56 57 58 59 60

for strain analysis of nanodevices[J]. Applied Physics Letters, 2008, 93(16).

[103] Grieb T, Krause F F, Schowalter M, et al. Strain analysis from nano-beam electron diffraction: Influence of specimen tilt and beam convergence[J]. Ultramicroscopy, 2018, 190: 45-57.

[104] Mahr C, Müller-Caspary K, Grieb T, et al. Theoretical study of precision and accuracy of strain analysis by nano-beam electron diffraction[J]. Ultramicroscopy, 2015, 158: 38-48.

[105] Ozdol V B, Gammer C, et al. Strain mapping at nanometer resolution using advanced nano-beam electron diffraction[J]. Applied Physics Letters, 2015, 106(25).

[106] Midgley P A , Sleight M E , Vincent R .The Structure of a Metastable Au–Sn Phase Determined by Convergent Beam Electron Diffraction[J].Journal of Solid State Chemistry, 1996, 124(1):132-142.

[107] Sinkler W , Marks L D , Edwards D D ,et al.Determination of Oxygen Atomic Positions in a Ga–In–Sn–O Ceramic Using Direct Methods and Electron Diffraction[J].Journal of Solid State Chemistry, 1998, 136(1):145-149.

[108] Vincent R , Midgley P A .Double conical beam-rocking system for measurement of integrated electron diffraction intensities[J].Ultramicroscopy, 1994, 53(3):271-282.

[109] Mahr C ,Müller-Caspary, Knut, Grieb T ,et al.Theoretical study of precision and accuracy of strain analysis by nano-beam electron diffraction[J].Ultramicroscopy, 2015, 158:38-48.

[110] Rauch E F , Portillo J , Nicolopoulos S ,et al.Automated nanocrystal orientation and phase mapping in the transmission electron microscope on the basis of precession electron diffraction[J].Zeitschrift für Kristallographie, 2010, 225(2).

[111] Kobler A , Kashiwar A , Hahn H ,et al.Combination of in situ straining and ACOM TEM: A novel method for analysis of plastic deformation of nanocrystalline metals[J].Ultramicroscopy, 2013, 128(Complete):68-81.

[112] Viladot D ,Véron,M, Gemmi M ,et al.Orientation and phase mapping in the transmission electron microscope using precession-assisted diffraction spot recognition: State-of-the-art results[J].Journal of Microscopy, 2013(1):252.

[113] Rauch E F, Véron M. Automated crystal orientation and phase mapping in TEM[J]. Materials Characterization, 2014, 98: 1-9.

[114] Rouviere J L, Béché A, Martin Y, et al. Improved strain precision with high spatial

Accepted Manuscript

resolution using nanobeam precession electron diffraction[J]. Applied Physics Letters, 2013, 103(24).

[115] Vigouroux M P, Delaye V, Bernier N, et al. Strain mapping at the nanoscale using precession electron diffraction in transmission electron microscope with off axis camera[J]. Applied Physics Letters, 2014, 105(19).

[116] Cooper D, Bernier N, Rouvière J L. Combining 2 nm spatial resolution and 0.02% precision for deformation mapping of semiconductor specimens in a transmission electron microscope by precession electron diffraction[J]. Nano letters, 2015, 15(8): 5289-5294.

[117] Eggeman A S, Krakow R, Midgley P A. Scanning precession electron tomography for three-dimensional nanoscale orientation imaging and crystallographic analysis[J]. Nature communications, 2015, 6(1): 7267.

[118] Bashir A, Millar R W, Gallacher K, et al. Strain analysis of a Ge micro disk using precession electron diffraction[J]. Journal of Applied Physics, 2019, 126(23).

[119] Goodman P, Lehmpfuhl G. Elektronenbeugungsuntersuchungen im konvergenten Bündel mit dem Siemens Elmiskop I[J]. Zeitschrift für Naturforschung A, 1965, 20(1): 110-114.

[120] Kossel W, Möllenstedt G. Elektroneninterferenzen im konvergenten Bündel[J]. Annalen der Physik, 1939, 428(2): 113-140.

[121] Goodman P. A practical method of three-dimensional space-group analysis using convergent-beam electron diffraction[J]. Acta Crystallographica Section A: Crystal Physics, Diffraction, Theoretical and General Crystallography, 1975, 31(6): 804-810.

[122] Tanaka M, Saito R, Sekii H. Point-group determination by convergent-beam electron diffraction[J]. Acta Crystallographica Section A: Foundations of Crystallography, 1983, 39(3): 357-368.

[123] Tanaka M. Convergent-beam electron diffraction[J]. Acta Crystallographica Section A: Foundations of Crystallography, 1994, 50(3): 261-286.

[124] Jones P M, Rackham G M, Steeds J W. Higher order Laue zone effects in electron diffraction and their use in lattice parameter determination[J]. Proceedings of the Royal Society of London. A. Mathematical and Physical Sciences, 1977, 354(1677): 197-222.

[125] Maher D M, Fraser H L, Humphreys C J, et al. Detection and measurement of local distortions in a semiconductor layered structure by convergent-beam electron diffraction[J].

Accepted Manuscript

1
2
3
4
5
6
7
8
9
10
11
12
13
14
15
16
17
18
19
20
21
22
23
24
25
26
27
28
29
30
31
32
33
34
35
36
37
38
39
40
41
42
43
44
45
46
47
48
49
50
51
52
53
54
55
56
57
58
59
60

Applied physics letters, 1987, 50(10): 574-576.

[126] Morawiec A. An algorithm for refinement of lattice parameters using CBED patterns[J]. Ultramicroscopy, 2007, 107(4-5): 390-395.

[127] Im S, Chen Z, Johnson J M, et al. Direct determination of structural heterogeneity in metallic glasses using four-dimensional scanning transmission electron microscopy[J]. Ultramicroscopy, 2018, 195: 189-193.

[128] Ophus C. Four-dimensional scanning transmission electron microscopy (4D-STEM): From scanning nanodiffraction to ptychography and beyond[J]. Microscopy and Microanalysis, 2019, 25(3): 563-582.

[129] Gammer C, Ophus C, Pekin T C, et al. Local nanoscale strain mapping of a metallic glass during in situ testing[J]. Applied Physics Letters, 2018, 112(17).

[130] Zewail A H. Four-dimensional electron microscopy[J]. science, 2010, 328(5975): 187-193.

[131] Zewail A H. 4D Visualization of Matter: Recent Collected Works of Ahmed H Zewail, Nobel Laureate[M]. World Scientific Publishing Company, 2014.

[132] Motoki K, Engel Z, Matthews C M, et al. Observation of interfacial strain relaxation and electron beam damage thresholds in $Al_{0.3}In_{0.7}N/GaN$ heterostructures by transmission electron microscopy[J]. Journal of Vacuum Science & Technology B, 2022, 40(5).

[133] Spessot A, Frabboni S, Balboni R, et al. Method for determination of the displacement field in patterned nanostructures by TEM/CBED analysis of split high-order Laue zone line profiles[J]. Journal of microscopy, 2007, 226(2): 140-155.

[134] Chuvilin A, Kaiser U. On the peculiarities of CBED pattern formation revealed by multislice simulation[J]. Ultramicroscopy, 2005, 104(1): 73-82.

[135] Ghamarian I, Liu Y, Samimi P, et al. Development and application of a novel precession electron diffraction technique to quantify and map deformation structures in highly deformed materials—as applied to ultrafine-grained titanium[J]. Acta Materialia, 2014, 79: 203-215.

[136] Avilov A, Kuligin K, Nicolopoulos S, et al. Precession technique and electron diffractometry as new tools for crystal structure analysis and chemical bonding determination[J]. Ultramicroscopy, 2007, 107(6-7): 431-444.

[137] Sharma R, Yang W C. Perspective and Prospects of In Situ Transmission/Scanning Transmission Electron Microscopy[J]. Microscopy, 2023: dfad057.

Accepted Manuscript

1
2
3
4
5
6
7
8
9
10
11
12
13
14
15
16
17
18
19
20
21
22
23
24
25
26
27
28
29
30
31
32
33
34
35
36
37
38
39
40
41
42
43
44
45
46
47
48
49
50
51
52
53
54
55
56
57
58
59
60

[138] Wang S, Eldred T B, Smith J G, et al. AutoDisk: Automated diffraction processing and strain mapping in 4D-STEM[J]. Ultramicroscopy, 2022, 236: 113513.

[139] Gabor D. Microscopy by reconstructed wave fronts: II[J]. Proceedings of the Physical Society. Section B, 1951, 64(6): 449.

[140] Haine M E, Mulvey T. The formation of the diffraction image with electrons in the Gabor diffraction microscope[J]. JOSA, 1952, 42(10): 763-773.

[141] DeVelis J B, Parrent G B, Thompson B J. Image reconstruction with Fraunhofer holograms[J]. JOSA, 1966, 56(4): 423-427.

[142] Haddad W S, Cullen D, Solem J C, et al. Fourier-transform holographic microscope[J]. Applied optics, 1992, 31(24): 4973-4978.

[143] Leith E N, Upatnieks J. Reconstructed wavefronts and communication theory[J]. JOSA, 1962, 52(10): 1123-1130.

[144] Möllenstedt G, Wahl H. Elektronenholographie und Rekonstruktion mit Laserlicht[J]. Naturwissenschaften, 1968, 55: 340-341

[145] Wahl H. Bildebenenholographie mit Elektronen[J]. Thesis Tubingen, 1975.

[146] Cowley J M. Twenty forms of electron holography[J]. Ultramicroscopy, 1992, 41(4): 335-348.

[147] Lichte H. Electron holography: optimum position of the biprism in the electron microscope[J]. Ultramicroscopy, 1996, 64(1-4): 79-86.

[148] Bragg W L. Microscopy by reconstructed wave-fronts[J]. Nature, 1950, 166(4218): 399-400.

[149] Crewe A V, Isaacson M, Johnson D. A simple scanning electron microscope[J]. Review of Scientific Instruments, 1969, 40(2): 241-246.

[150] Li L, Hu X, Gao Y. Electron Holographic Study of Semiconductor Light-Emitting Diodes[J]. Small, 2018, 14(6): 1701996.

[151] Chen J, Hirayama T, Lai G, et al. Real-time electron-holographic interference microscopy with a liquid-crystal spatial light modulator[J]. Optics letters, 1993, 18(22): 1887-1889.

[152] Lai G, Hirayama T, Ishizuka K, et al. Three-dimensional reconstruction of electric-potential distribution in electron-holographic interferometry[J]. Applied optics, 1994, 33(5): 829-833.

[153] Yamamoto K, Kawajiri I, Tanji T, et al. High precision phase-shifting electron

Accepted Manuscript

1
2
3
4
5
6
7
8
9
10
11
12
13
14
15
16
17
18
19
20
21
22
23
24
25
26
27
28
29
30
31
32
33
34
35
36
37
38
39
40
41
42
43
44
45
46
47
48
49
50
51
52
53
54
55
56
57
58
59
60

holography[J]. Microscopy, 2000, 49(1): 31-39.

[154] Mánuel J M, Koch C T, Özdöl V B, et al. Inline electron holography and VEELS for the measurement of strain in ternary and quaternary (In, Al, Ga) N alloyed thin films and its effect on bandgap energy[J]. Journal of Microscopy, 2016, 261(1): 27-35.

[155] Song K, Shin G Y, Kim J K, et al. Strain mapping of LED devices by dark-field inline electron holography: Comparison between deterministic and iterative phase retrieval approaches[J]. Ultramicroscopy, 2013, 127: 119-125.

[156] Hÿtch M, Houdellier F, Hüe F, et al. Nanoscale holographic interferometry for strain measurements in electronic devices[J]. Nature, 2008, 453(7198): 1086-1089

[157] Williams D B, Carter C B. Transmission electron microscopy: a textbook for materials science[J]. Micron, 1997, 28(1): 75-75.

[158] Hirsch P B, Whelan M J. A kinematical theory of diffraction contrast of electron transmission microscope images of dislocations and other defects[J]. Philosophical Transactions of the Royal Society of London. Series A, Mathematical and Physical Sciences, 1960, 252(1017): 499-529.

[159] Howie A, Whelan M J. Diffraction contrast of electron microscope images of crystal lattice defects. III. Results and experimental confirmation of the dynamical theory of dislocation image contrast[J]. Proceedings of the Royal Society of London. Series A. Mathematical and Physical Sciences, 1962, 267(1329): 206-230.

[160] Cockayne D J H, Ray I L F, Whelan M J. Investigations of dislocation strain fields using weak beams[J]. Philosophical Magazine, 1969, 20(168): 1265-1270.

[161] Barnard J S, Sharp J, Tong J R, et al. Three-dimensional analysis of dislocation networks in GaN using weak-beam dark-field electron tomography[J]. Philosophical Magazine, 2006, 86(29-31): 4901-4922.

[162] Aristov V V, Zaretskii A V, Osipyan Y A, et al. Dislocations in deformed ZnSe single crystals as studied by Weak-beam electron microscopy[J]. physica status solidi (a), 1983, 75(1): 101-106.

[163] Yao B, Heinrich H, Smith C, et al. Hollow-cone dark-field transmission electron microscopy for dislocation density characterization of trimodal Al composites[J]. Micron, 2011, 42(1): 29-35.

Accepted Manuscript

1
2
3
4
5
6
7
8
9
10
11
12
13
14
15
16
17
18
19
20
21
22
23
24
25
26
27
28
29
30
31
32
33
34
35
36
37
38
39
40
41
42
43
44
45
46
47
48
49
50
51
52
53
54
55
56
57
58
59
60

[164] Phillips P J, Mills M J, De Graef M. Systematic row and zone axis STEM defect image simulations[J]. Philosophical Magazine, 2011, 91(16): 2081-2101.

[165] Cockayne D J H. The principles and practice of the weak-beam method of electron microscopy[J]. Journal of Microscopy, 1973, 98(2): 116-134.

[166] Wu F, Sun H, AJia I A, et al. Significant internal quantum efficiency enhancement of GaN/AlGaN multiple quantum wells emitting at~ 350 nm via step quantum well structure design[J]. Journal of Physics D: Applied Physics, 2017, 50(24): 245101.

[167] S. J. Pennycook and D. E. Jesson, High-resolution Z-contrast imaging of crystals[J], Ultramicroscopy, 1991, 37(1–4), 14–38

[168] J. Loos, E. Sourty, K. Lu, G. de With and S. V. Bavel, Imaging Polymer Systems with High-Angle Annular Dark Field Scanning Transmission Electron Microscopy (HAADF-STEM)[J], Macromolecules, 2009, 42(7), 2581–2586 .

[169] Sohlberg K, Pennycook T J, Zhou W, et al. Insights into the physical chemistry of materials from advances in HAADF-STEM[J].Physical Chemistry Chemical Physics 17.6 (2015): 3982-4006.

[170] S. J. Pennycook, Z-contrast STEM for materials science[J], Ultramicroscopy, 1989, 30(1–2), 58–69 .

[171] Feng Q, Zhu Y, Hong J, et al. Growth of large-area 2D $MoS_{2(1-x)}Se_{2x}$ semiconductor alloys[J]. Advanced Materials 26.17 (2014): 2648-2653.

[172] Bertoni G, Grillo V, Brescia R, et al. Direct determination of polarity, faceting, and core location in colloidal core/shell wurtzite semiconductor nanocrystals[J]. ACS nano 6.7 (2012): 6453-6461.

[173] Hong, J W, et al. Metal–semiconductor heteronanocrystals with desired configurations for plasmonic photocatalysis[J]. Journal of the American Chemical Society 138.48 (2016): 15766-15773.

[174] S. J. Pennycook. Structure determination through Z-contrast microscopy[M]//Advances in imaging and electron physics. Elsevier, 2002, 123: 173-206.

[175] T. Walther: A new experimental procedure to quantify annular dark field images in scanning transmission electron microscopy.[J]. Microsc. 221:2 (2006) 137-144.

[176] Nellist, P. D., and S. J. Pennycook. The principles and interpretation of annular dark-field

Accepted Manuscript

1
2
3
4
5
6
7
8
9
10
11
12
13
14
15
16
17
18
19
20
21
22
23
24
25
26
27
28
29
30
31
32
33
34
35
36
37
38
39
40
41
42
43
44
45
46
47
48
49
50
51
52
53
54
55
56
57
58
59
60

Z-contrast imaging[J].Advances in imaging and electron physics. Vol. 113. Elsevier, 2000. 147-203.

[177] T. Walther, C.J. Humphreys, D.J. Robbins: Diffusion and surface segregation in thin SiGe / Si layers studied by scanning transmission electron microscopy. Defect and Diffusion Forum 143-147 (1997) 1135-1140.

[178] T. Walther, H. Amari, I.M. Ross, T. Wang, A.G. Cullis: Lattice resolved annular dark-field scanning transmission electron microscopy of (Al, In)GaN / GaN layers for measuring segregation with sub-monolayer precision. Mater. Sci. 48 (2013) 2883-2892.

[179] T. Walther, C.J. Humphreys: Quantification of the composition of silicon germanium / silicon structures by high-angle annular dark field imaging. Proc. EMAG97, Cambridge. Inst. Phys. Conf. Ser. 153 (1997) 303-306.

[180] Muralt P. AlN thin film processing and basic properties[J]. Piezoelectric MEMS resonators, 2017: 3-37.

[181] Ishihara M, Li S J, Yumoto H, et al. Control of preferential orientation of AlN films prepared by the reactive sputtering method[J]. Thin Solid Films, 1998, 316(1-2): 152-157.

[182] Pinto R M R, Gund V, Dias R A, et al. CMOS-Integrated aluminum nitride MEMS: A review[J]. Journal of Microelectromechanical Systems, 2022, 31(4): 500-523.

[183] Beshkova M, Yakimova R. Properties and potential applications of two-dimensional AlN[J]. Vacuum, 2020, 176: 109231.

[184] Iriarte G F, Rodríguez J G, Calle F. Synthesis of c-axis oriented AlN thin films on different substrates: A review[J]. Materials Research Bulletin, 2010, 45(9): 1039-1045.

[185] Tang B, Hu H, Wan H, et al. Growth of high-quality AlN films on sapphire substrate by introducing voids through growth-mode modification[J]. Applied Surface Science, 2020, 518: 146218.

[186] Xu F J, Zhang L S, Xie N, et al. Realization of low dislocation density AlN on a small-coalescence-area nano-patterned sapphire substrate[J]. CrystEngComm, 2019, 21(15): 2490-2494.

[187] Dovidenko K, Oktyabrsky S, Narayan J. Characteristics of stacking faults in AlN thin films[J]. Journal of applied physics, 1997, 82(9): 4296-4299.

[188] Bai J, Wang T, Parbrook P J, et al. A study of dislocations in AlN and GaN films grown on

Accepted Manuscript

1
2
3
4
5
6
7
8
9
10
11
12
13
14
15
16
17
18
19
20
21
22
23
24
25
26
27
28
29
30
31
32
33
34
35
36
37
38
39
40
41
42
43
44
45
46
47
48
49
50
51
52
53
54
55
56
57
58
59
60

sapphire substrates[J]. Journal of crystal growth, 2005, 282(3-4): 290-296.

[189] Stampfl C, Van de Walle C G. Energetics and electronic structure of stacking faults in AlN, GaN, and InN[J]. Physical Review B, 1998, 57(24): R15052.

[190] Meng F, Estruga M, Forticaux A, et al. Formation of stacking faults and the screw dislocation-driven growth: a case study of aluminum nitride nanowires[J]. Acs Nano, 2013, 7(12): 11369-11378.

[191] Vahidi, H. , et al. A Review of Grain Boundary and Heterointerface Characterization in Polycrystalline Oxides by (Scanning) Transmission Electron Microscopy[J].Crystals (2021).

[192] P. Schiske, Proceedings of the Fourth European Conference on Electron Microscopy, Rome, 1968, p. 145.

[193] Van Dyck D, Op de Beek M, Coene W. A new approach to object wavefunction reconstruction in electron microscopy[J]. Optik (Stuttgart), 1993, 93(3): 103-107.

[194] Kawasaki, Tadahiro , et al. Wave field restoration using three-dimensional Fourier filtering method[J]. 90.1(2001):47-59.

[195] Dah-Min David Hwang, Strain relaxation in lattice-mismatched epitaxy[J], Materials Chemistry and Physics, 40, 1995, 291-297.

[196] Matthews J W, Blakeslee A E. Defects in epitaxial multilayers: II. Dislocation pile-ups, threading dislocations, slip lines and cracks[J]. Journal of Crystal Growth, 1975, 29(3): 273-280.

[197] Findlay, S. D., et al. Dynamics of annular bright field imaging in scanning transmission electron microscopy[J]. Ultramicroscopy 110.7 (2010): 903-923.

[198] Okunishi, E , et al. Visualization of Light Elements at Ultrahigh Resolution by STEM Annular Bright Field Microscopy[J].Microscopy & Microanalysis 15.S2(2009):164-165.

[199] Shao-Horn, Y., et al. Atomic resolution of lithium ions in $LiCoO_2$[J]. Nature Mater. 2, 464–467 (2003).

[200] Alexeev E M, Catanzaro A, Skrypka O V, et al. Imaging of interlayer coupling in van der Waals heterostructures using a bright-field optical microscope[J]. Nano letters, 2017, 17(9): 5342-5349.

[201] Petroff P M. Transmission electron microscopy of interfaces in III–V compound semiconductors[J]. Journal of Vacuum Science and Technology, 1977, 14(4): 973-978.

[202] Liu H Y, et al. 1.55 μm InAs quantum dots grown on a GaAs substrate using a GaAsSb

Accepted Manuscript

metamorphic buffer layer[J]. Applied Physics Letters, 2008, 92(11).

[203] Rafferty B, Brown L M. Direct and indirect transitions in the region of the band gap using electron-energy-loss spectroscopy[J]. Physical Review B, 1998, 58(16): 10326.

[204] Aguiar J A, Reed B W, Ramasse Q M, et al. Quantifying the low-energy limit and spectral resolution in valence electron energy loss spectroscopy[J]. Ultramicroscopy, 2013, 124: 130-138.

[205] Yuan J, Brown L M, Liang W Y. Electron energy-loss spectroscopy of the high-temperature superconductor $Ba_2YCu_3O_{7-x}$[J]. Journal of Physics C: Solid State Physics, 1988, 21(3): 517.

[206] French R H, Müllejans H, Jones D J, et al. Dispersion forces and Hamaker constants for intergranular films in silicon nitride from spatially resolved-valence electron energy loss spectrum imaging[J]. Acta Materialia, 1998, 46(7): 2271-2287.

[207] TERAUCHI, TANAKA, TSUNO, et al. Development of a high energy resolution electron energy-loss spectroscopy microscope[J]. Journal of microscopy, 1999, 194(1): 203-209.

[208] Benner G, Essers E, Matijevic M, et al. Performance of monochromized and aberration-corrected TEMs[J]. Microscopy and Microanalysis, 2004, 10(S02): 108-109.

[209] Brink H A, Barfels M M G, Burgner R P, et al. A sub-50 meV spectrometer and energy filter for use in combination with 200 kV monochromated (S) TEMs[J]. Ultramicroscopy, 2003, 96(3-4): 367-384.

[210] Lazar S, Botton G A, Wu M Y, et al. Materials science applications of HREELS in near edge structure analysis and low-energy loss spectroscopy[J]. Ultramicroscopy, 2003, 96(3-4): 535-546.

[211] Arslan I, Ogut S, Nellist P D, et al. Comparison of simulation methods for electronic structure calculations with experimental electron energy-loss spectra[J]. Micron, 2003, 34(3-5): 255-260.

[212] Lazar S, Botton G A, Zandbergen H W. Enhancement of resolution in core-loss and low-loss spectroscopy in a monochromated microscope[J]. Ultramicroscopy, 2006, 106(11-12): 1091-1103.

[213] Rafferty B, Brown L M. Direct and indirect transitions in the region of the band gap using electron-energy-loss spectroscopy[J]. Physical Review B, 1998, 58(16): 10326.

[214] Rafferty B, Pennycook S J, Brown L M. Zero loss peak deconvolution for bandgap EEL spectra[J]. Microscopy, 2000, 49(4): 517-524.

Accepted Manuscript

[215] Schamm S, Zanchi G. Study of the dielectric properties near the band gap by VEELS: gap measurement in bulk materials[J]. Ultramicroscopy, 2003, 96(3-4): 559-564.

[216] Stöger-Pollach M, Franco H, Schattschneider P, et al. Čerenkov losses: A limit for bandgap determination and Kramers–Kronig analysis[J]. Micron, 2006, 37(5): 396-402.

[217] Roessler D M. Kramers-Kronig analysis of reflection data[J]. British Journal of Applied Physics, 1965, 16(8): 1119.

[218] R Erni, N D Browning. The impact of surface and retardation losses on valence electron energy-loss spectroscopy[J]. Ultramicrosc. 2008，108, 84–99 .

[219] K. Kimoto, G. Kothleitner, W. Grogger, Y. Matsui, F. Hofer. Advantages of a monochromator for bandgap measurements using electron energy-loss spectroscopy[J]. Micron，2005，36, 185.

[220] Brodusch N, Demers H, Gellé A, et al. Electron energy-loss spectroscopy (EELS) with a cold-field emission scanning electron microscope at low accelerating voltage in transmission mode[J]. Ultramicroscopy, 2019, 203: 21-36.

[221] T. Walther, E. Quandt, H. Stegmann, A. Thesen, G. Benner: First experimental test of a new monochromated and aberration-corrected 200kV field-emission scanning transmission electron microscope[J]. Ultramicroscopy 106:11-12 (2006) 936-939.

[222] Mizoguchi T, Miyata T, Olovsson W. Excitonic, vibrational, and van der Waals interactions in electron energy loss spectroscopy[J]. Ultramicroscopy, 2017, 180: 93-103.

[223] Colliex C, Kociak M, Stéphan O. Electron energy loss spectroscopy imaging of surface plasmons at the nanometer scale[J]. Ultramicroscopy, 2016, 162: A1-A24.

[224] X. Wang, M.-P. Chauvat, P. Ruterana, T. Walther: Investigation of phase separation in InGaN alloys by plasmon loss spectroscopy in TEM [J]. MRS Advances 1:40 (2016) 2749-2756.

[225] T. Walther: Comment on 'Nanoscale mapping of optical band gaps using monochomated electron energy loss spectroscopy' by Zhan, Granerod, Venkatachalapathy, Johansen, Jensen, Kuznetsov and Prytz. Nanotechnology 29:31 (2018) 318001.

[226] Bosman M, Tang L J, Ye J D, et al. Nanoscale band gap spectroscopy on ZnO and GaN-based compounds with a monochromated electron microscope[J]. Applied Physics Letters, 2009, 95(10).

[227] Gorczyca I, Łepkowski S P, Suski T, et al. Influence of indium clustering on the band

Accepted Manuscript

1
2
3
4
5
6
7
8
9
10
11
12
13
14
15
16
17
18
19
20
21
22
23
24
25
26
27
28
29
30
31
32
33
34
35
36
37
38
39
40
41
42
43
44
45
46
47
48
49
50
51
52
53
54
55
56
57
58
59
60

structure of semiconducting ternary and quaternary nitride alloys[J]. Physical Review B, 2009, 80(7): 075202.

[228] Collins G B, Reiling V G. Čerenkov radiation[J]. Physical Review, 1938, 54(7): 499.

[229] Sinclair, R., In situ high-resolution transmission electron microscopy of material reactions[J]. Mrs Bulletin 2013, 38 (12), 1065-1071.

[230] Sinclair, R., et al. The development of in situ high-resolution electron microscopy[J]. Acta Crystallographica Section A: Foundations of Crystallography 44.6 (1988): 965-975.

[231] Taheri, Mitra L., et al. Laser-based in situ techniques: Novel methods for generating extreme conditions in TEM samples[J]. Microscopy research and technique 72.3 (2009): 122-130.

[232] Ko, Dae-Hong, and Robert Sinclair. In-situ dynamic high-resolution transmission electron microscopy: application to Pt/GaAs interfacial reactions[J]. Ultramicroscopy 54.2-4 (1994): 166-178.

[233] Sharma, R., Experimental set up for in situ transmission electron microscopy observations of chemical processes[J]. Micron 2012, 43 (11), 1147-1155.

[234] Shan, Z. W.; Mishra, R. K.; Asif, S. A. S.; Warren, O. L.; Minor, A. M., Mechanical annealing and source-limited deformation in submicrometre-diameter Ni crystals[J]. Nature materials 2008, 7 (2), 115-119.

[235] Pu S, Gong C, Robertson A W. Liquid cell transmission electron microscopy and its applications[J]. Royal Society open science, 2020, 7(1): 191204.

[236] McDowell M T, Jungjohann K L, Celano U. Dynamic nanomaterials phenomena investigated with in situ transmission electron microscopy: A nano letters virtual issue[J]. Nano Letters, 2018, 18(2): 657-659.

[237] Creemer J F, Helveg S, Kooyman P J, et al. A MEMS reactor for atomic-scale microscopy of nanomaterials under industrially relevant conditions[J]. Journal of Microelectromechanical Systems, 2010, 19(2): 254-264.

[238] Hetherington C, Jacobsson D, Dick K A, et al. In situ metal-organic chemical vapour deposition growth of III–V semiconductor nanowires in the Lund environmental transmission electron microscope[J]. Semiconductor Science and Technology, 2020, 35(3): 034004.

[239] Allard, Lawrence F., et al. Novel MEMS-based gas-cell/heating specimen holder provides advanced imaging capabilities for in situ reaction studies[J]. Microscopy and Microanalysis 18.4

Accepted Manuscript

1
2
3
4
5
6
7
8
9
10
11
12
13
14
15
16
17
18
19
20
21
22
23
24
25
26
27
28
29
30
31
32
33
34
35
36
37
38
39
40
41
42
43
44
45
46
47
48
49
50
51
52
53
54
55
56
57
58
59
60

(2012): 656-666.

[240] Zewail, A. H., 4D ultrafast electron diffraction, crystallography, and microscopy[J]. In Annual Review of Physical Chemistry, 2006; Vol. 57, pp 65-103.

[241] Bostanjoglo, O.; Horinek, W. R., Pulsed TEM-a new method to detect transient structures in fast phase-transitions[J]. Optik 1983, 65 (4), 361-367.

[242] Liao, Hong-Gang, et al. Real-time imaging of Pt_3Fe nanorod growth in solution[J]. science 336.6084 (2012): 1011-1014.

[243] Liao,Hong-Gang,etal.Facet development during platinum nanocube growth[J]. science 345.6199 (2014): 916-919.

[244] Han, Myung-Geun, et al. Interface-induced nonswitchable domains in ferroelectric thin films[J]. Nature communications 5.1 (2014): 4693.

[245] Yuan, Yifei, et al. Understanding materials challenges for rechargeable ion batteries with in situ transmission electron microscopy[J]. Nature communications 8.1 (2017): 15806.

[246] Liu, Zhilin, et al. Nanomechanical behavior of single taper-free GaAs nanowires unravelled by in-situ TEM mechanical testing and molecular dynamics simulation[J]. Materials Science and Engineering: A 806 (2021): 140866.

[247] Gott, James A., et al. Defect dynamics in self-catalyzed III-V semiconductor nanowires[J]. Nano Letters 19.7 (2019): 4574-4580.

[248] Leamy, H. J., et al. Explosive crystallization of amorphous germanium[J]. Applied Physics Letters 38.3 (1981): 137-139.

[249] Fitzgerald, A. G. Electron beam crystallization of amorphous germanium films in the electron microscope[J]. Journal of Materials Science Letters 1.4 (1982): 145-146.

[250] Egan, G., et al. In situ dynamic transmission electron microscopy characterization of liquid-mediated crystallization of amorphous Ge[J]. Journal of Applied Physics 126.10 (2019).

[251] Sharma, R. K., et al. Electron beam induced explosive crystallization of unsupported amorphous germanium thin films[J]. Journal of applied physics 55.2 (1984): 387-394.

[252] Shahrjerdi, Davood, et al. Low temperature stress-induced crystallization of germanium on plastic[J]. Thin Solid Films 427.1-2 (2003): 330-334.

[253] Radnoczi, Gy, and B. Pécz. Crystallization of encapsulated very thin amorphous Ge layers[J].Thin Solid Films 232.1 (1993): 68-72.

Accepted Manuscript

1 2 3 4 5 6 7 8 9 10 11 12 13 14 15 16 17 18 19 20 21 22 23 24 25 26 27 28 29 30 31 32 33 34 35 36 37 38 39 40 41 42 43 44 45 46 47 48 49 50 51 52 53 54 55 56 57 58 59 60

[254] Okabe, Toshio, Yoshihiro Kagawa, and Syoso Takai. High resolution electron microscopic observation on a pentagonal nucleus formed in amorphous germanium films[J]. Philosophical magazine letters 63.4 (1991): 233-239.

[255] Knaepen, Werner, et al. In situ X-ray diffraction study of metal induced crystallization of amorphous germanium[J]. Journal of Applied Physics 105.8 (2009).

[256] Kryshtal A, Bogatyrenko S, Ferreira P. Metal-induced crystallization of amorphous semiconductor films: Nucleation phenomena in Ag-Ge films[J]. Applied Surface Science 606 (2022): 154873.

[257] Zhu, Guo-zhen, et al. Atomic-level 2-dimensional chemical mapping and imaging of individual dopants in a phosphor crystal[J]. Physical Chemistry Chemical Physics 15.27 (2013): 11420-11426.

[258] Yu,X.Z.,etal.Real-space observation of a two-dimensional skyrmion crystal [J]. Nature 465.7300 (2010): 901-904.

[259] Yoshida, Hideto, et al. Visualizing gas molecules interacting with supported nanoparticulate catalysts at reaction conditions[J]. Science 335.6066 (2012): 317-319.

[260] Wall, M. A.; Dahmen, U., An in situ nanoindentation specimen holder for a high voltage transmission electron microscope[J]. Microscopy Research and Technique 1998, 42 (4), 248-254.

[261] Legros, M.; Gianola, D. S.; Hemker, K. J., In situ TEM observations of fast grain-boundary motion in stressed nanocrystalline aluminum films[J]. Acta Mater. 2008, 56 (14), 3380-3393.

[262] Henderson M A. The influence of oxide surface structure on adsorbate chemistry: Desorption of water from the smooth, the microfaceted and the ion sputtered surfaces of TiO_2 (100)[J]. Surface science, 1994, 319(3): 315-328.

[263] T. Walther: What environmental transmission electron microscopy measures and how this links for diffusivity: thermodynamic versus kinetics.[J] Microsc. 257:2 (215) 87-91.

[264] Winterstein, J., Lin, Pin Ann, Sharma, R, Temperature Calibration for In Situ Environmental Transmission Electron Microscopy Experiments[J]. Microscopy and Microanalysis 2015, First view, 1-7.

[265] Vendelbo, S. B.; Kooyman, P. J.; Creemer, J. F.; Morana, B.; Mele, L.; Dona, P.; Nelissen, B. J.; Helveg, S., Method for local temperature measurement in a nanoreactor for in situ high-resolution electron microscopy[J]. Ultramicroscopy 2013, 133, 72-79.

Accepted Manuscript

1
2
3
4
5
6
7
8
9
10
11
12
13
14
15
16
17
18
19
20
21
22
23
24
25
26
27
28
29
30
31
32
33
34
35
36
37
38
39
40
41
42
43
44
45
46
47
48
49
50
51
52
53
54
55
56
57
58
59
60
Accepted Manuscript